Department of Physics and Astronomy
University of Heidelberg

Master thesis

in Physics

submitted by

Felix Maximilian Klein

born in Münchweiler an der Alsenz

2024

Nonlinear Spin Dynamics Initiated by Local Control of the Spinor Phase in a Bose-Einstein Condensate

This Master thesis has been carried out by Felix Maximilian Klein

at the

Kirchhoff -Institut für Physik

under the supervision of

Prof. Dr. Markus K. Oberthaler

Abstract

This thesis reports on local manipulation of the spin state of a quasi–one–dimensional spinor Bose–Einstein condensate (BEC) of ^{87}Rb atoms. Utilizing the existing laser setup for local control in a novel way enables us to perform local spinor phase rotations on the BEC. Subsequent laser pulses allow for the imprinting of spatial structures, with a resolution of (5.7 ± 0.7)µm. We investigate the temporal evolution of spatially flat initial conditions under different settings for the second–order Zeeman shift. The system evolves locally as predicted by the single–mode approximation (SMA), supporting the use of the local density approximation (LDA). Comparing the oscillations in the relative populations of the side–modes to a simulation of the SMA, we extract effective values for the spin-spin interaction (1.5 ± 0.1)Hz and the second–order Zeeman shift. The latter depends linearly on the experimentally programmed value, with a slope of 1.07 ± 0.07. Further analysis of spin dynamics with local spinor phase rotations highlights deviations from the LDA and investigates the conditions for the deterministic preparation of a vortex in the transversal spin in space and time. We show first experiments towards the deterministic preparation of such structures.

Zusammenfassung

Diese Arbeit beschreibt die lokale Manipulation des Spinzustands eines quasi eindimensionalen Spinor-Bose-Einstein-Kondensats (BEC) aus ^{87}Rb Atomen. Durch die neuartige Nutzung des vorhandenen Laseraufbaus zur lokalen Kontrolle können wir lokale Spinorphasenrotationen an dem BEC durchführen. Aufeinanderfolgende Laserpulse ermöglichen das Aufprägen von räumlichen Strukturen mit einer Auflösung von $(5,7 \pm 0,7)$µm. Wir untersuchen die zeitliche Entwicklung von räumlich flachen Anfangsbedingungen unter verschiedenen Einstellungen für die Zeeman-Verschiebung zweiter Ordnung. Das System entwickelt sich lokal, wie von der single–mode–approximation (SMA) vorhergesagt, was die Verwendung der local density approximation (LDA) unterstützt. Durch Vergleich der Oszillationen der relativen Populationen in den Seitenmoden mit einer Simulation der SMA extrahieren wir effektive Werte für die Spin-Spin-Wechselwirkung $(1,5 \pm 0,1)$Hz und die Zeeman-Verschiebung zweiter Ordnung. Letztere hängt linear vom experimentell programmierten Wert ab, mit einer Steigung von 1.07 ± 0.07. Eine weitere Analyse der Spindynamik mit lokalen Spinor-Phasendrehungen zeigt Abweichungen von der LDA auf und untersucht die Bedingungen für die deterministische Vorbereitung eines Wirbels im Transversalen Spin in Raum und Zeit. Wir zeigen erste Experimente zur deterministischen Präparation solcher Strukturen.

Contents

1 Introduction **5**

2 Theoretical background **7**
2.1 The spin-1 system . . . 7
2.2 Mean–field description and GPE . . . 9
2.3 Mean–field dynamics in the single–mode approximation . . . 10
2.4 Phase diagram and post quench dynamics . . . 13

3 Experimental system **16**

4 Local control of the spinor phase **19**
4.1 Method for local spinor phase rotations . . . 19
4.2 Experimental analysis of the state preparation . . . 21
4.2.1 Background oscillation . . . 21
4.2.2 Analysis of shape and depth of the local imprint . . . 22

5 Global spin dynamics **26**
5.1 Control of the second–order Zeemann shift . . . 26
5.2 Experimental investigation of spin dynamics . . . 27

6 Spin dynamics with local spinor phase rotation **34**
6.1 Local spin oscillation . . . 34
6.2 Leaving the trapped region locally . . . 36
6.3 Towards creating a vortex in the Larmor phase . . . 38

7 Conclusion and outlook **44**

A Simulation SMA **49**

B Additional plots to Section 5 **50**

C Additional plots to Section 6.3 **53**

1 Introduction

In recent years, there has been significant interest in studying quantum many-body systems far from equilibrium [1–3]. The behavior of these systems provides a valuable opportunity to gain deeper insights into mechanisms that are believed to be universal and govern the time evolution of various physical configurations, such as quark–gluon plasma or the early universe [4, 5]. The study of dynamics far from equilibrium is particularly interesting due to the complexity arising from interaction on different length scales. A common example of this is turbulence in classical hydrodynamics, where kinetic energy is transported towards small length scales, associated with the self–similar eddie–like structure, and eventually dissipated into the system as heat at the Kolmogorov microscale [6].

Isolated ultra-cold quantum many-body systems, such as Bose-Einstein condensates (BECs), offer an exceptional platform for exploring and simulating far-from-equilibrium physics [7]. These systems are highly controllable and can be used to study and simulate certain Hamiltonians, making them ideal candidates for investigating complex many-body phenomena that can be challenging to access through classical computational simulations. Spinor BECs, which consist of multiple components corresponding to different magnetic sub-levels, are especially interesting. The interactions in their spin degree of freedom allow the observation of phenomena such as phase transitions [8], spin–mixing dynamics [9], and spin domain formation [10] along with its subsequent coarsening dynamics [11].

The experiments presented in this thesis are performed with a quasi one–dimensional spinor BEC. One phenomenon that has been observed in this setup is universal dynamics near a non–thermal fixed point [12]. A numerical study [13] has investigated the relation of this behavior to the presence of vortices in both space and time, in the complex order parameter in the easy-plane phase, that is, the transversal spin field $F_\perp$. The vortices show up stochastically in the scaling regime, which means they can not be observed in the experiment, as each measurement is a snapshot of a different realization of the experiment.

We aimed to prepare such a vortex deterministically in the experiment. For this we developed a method to prepare states with spatially varying transversal spin length, which constitutes a new class of initial condition than previously studied in the experiment. This method uses a steerable laser that locally illuminates the atom cloud, causing a relative shift of the spinor phase with respect to the rest of the condensate. The latter can be visually understood, as it “rotates” a state from an elongated transversal spin into a quadrupole moment, that is, reducing the spin length.

Besides the spatial control of the spinor phase, precise knowledge and control of the parameters governing the spin dynamics is key for the deterministic generation of such a vortex. For this, we investigate the time evolution of spatially flat spin profiles, which can be locally understood by means of the single–mode approximation. We compare the measured trajectories in spin space with a simulation of the latter to extract effective parameters for the second–order Zeemann shift and the spin–spin interaction. Our findings demonstrate how the local imprint on the spin length causes the system to deviate from the behavior expected under the single–mode approximation.

Section 2 gives an overview of the theoretical background behind the presented

work. After introducing the single–particle spin–1 system, we move on to the Gross–Pitaevski equation, describing the spinor BEC on a mean field level. After that, the focus is on the systems internal spin dynamics. Section 2.3, shows results of a simulation of the equations of motion for the spin degree of freedom in the single–mode approximation. Finally, the phase diagram is shown, and a very brief overview over previous studies investigating the dynamics after a quench from the polar to the easy–plane phase is given.

Section 3 briefly presents the experimental setup. The level scheme of ^{87}Rb is shown, and the different control techniques for manipulating and extracting the internal spin states are described.

Section 4 presents the method for the local control of the spinor phase. The depth and shape of the prepared spin profiles are then investigated in the experiment.

In **Section 5**, the experimental control of the effective second–order Zeeman shift is briefly explained. It relies on a calibration based on a simplified model. The actual value q_{eff} may still differ significantly with respect to the spin interaction strength, so its independent measurement is highly desirable.

To do so, the time evolution of spatially flat spin profiles is observed with different values for q_{eff}. The measured oscillations are used to obtain the values for the latter, as well as an effective value for the spin–spin interaction strength $\tilde{c}_1$, by a comparison to the spin equations of motion in the single–mode approximation, that is, assuming no spatial spin structure.

Section 6 observes, how the dynamic behavior changes when the initial condition features a local rotation in the spinor phase. For a small rotation, the system locally still resembles the trajectories expected from the single–mode approximation, while for a larger imprint, the system behaves very differently, as kinetic energy becomes more relevant. Finally, we present the results of a measurement that so far holds the most promise for observing a vortex in the transverse spin $F_\perp$.

2 Theoretical background

In order to describe the many-body state of a spin-1 BEC, it is instructive to first gain an understanding of the theoretical description of a spin-1 system on the single-particle level. Even though what we finally aim to describe is a one-dimensional many–body state, the relevant observables can be understood on a single–particle level. As we aim to describe the dynamics of the spinor BEC on the mean-field level, we then introduce the mean-field equation of motion, that is the Gross-Pitaevskii equation. Finally we will discuss the spin dynamics in the single-mode approximation and the resulting ground–state phase diagram. This chapter is based on [14–16].

2.1 The spin-1 system

The experiments in this thesis are performed in the F=1 hyperfine manifold of ^{87}Rb, with F being the total angular momentum quantum number of the single atoms, respecting the internal coupling of the nuclear spin and the spin of the electron. This section aims to introduce the graphical representation of a single particle spin–1 state and the relevant observables.

A spin-1 state is described by a normalized, three component, complex valued vector. It can be parametrized via

$$|\psi\rangle = r_1 e^{i\phi_L/2}|1\rangle + r_0 e^{i\phi_S}|0\rangle + r_{-1}e^{-i\phi_L/2}|-1\rangle = \begin{pmatrix} r_1 e^{i\phi_L/2} \\ r_0 e^{i\phi_S} \\ r_{-1}e^{-i\phi_L/2} \end{pmatrix}, \tag{1}$$

with Larmor phase $\phi_L = \varphi_1 - \varphi_{-1}$ and spinor phase $\phi_S = \varphi_0 - (\varphi_1 + \varphi_{-1})/2$, where φ_m are the phases of the three magnetic substates $|m_f\rangle$. The role of Larmor and spinor phase is important in this work, and can intuitively be understood as will be discussed in the following. As in a spin 1/2 system, the spin 1 state can be visualized as a point on the spin sphere (see fig. 1, left) with the well-known role of the Larmor phase as the polar angle. However, in contrast to the spin 1/2 system, even a pure spin 1 state does not necessarily lie on the surface, but can correspond to any point within the sphere. Furthermore, the coordinates in this visualization, representing the expectation values for the three spin observables, are not sufficient to fully describe a spin 1 state. This is due to the fact that, in contrast to the spin 1/2 system, there are more than the three operators that form an operator basis for the hermitian observables of the spin-1 system. In addition to the spin 1 analog of the three spin operators

$$\hat{S}_x = \frac{1}{\sqrt{2}}\begin{pmatrix} 0 & 1 & 0 \\ 1 & 0 & 1 \\ 0 & 1 & 0 \end{pmatrix}, \hat{S}_y = \frac{1}{\sqrt{2}}\begin{pmatrix} 0 & -i & 0 \\ i & 0 & i \\ 0 & -i & 0 \end{pmatrix} \text{ and } \hat{S}_z = \begin{pmatrix} 1 & 0 & 0 \\ 0 & 0 & 0 \\ 0 & 0 & -1 \end{pmatrix}, \tag{2}$$

which fulfill the su(2) commutation relation $[\hat{S}_i, \hat{S}_j] = i\epsilon_{ijk}\hat{S}_k$, and are thus generators of rotations on the sphere spanned by their expectation values, a convenient choice to describe the spin-1 system are the quadrupole operators $\hat{Q}_{ij} = \hat{S}_i\hat{S}_j + \hat{S}_j\hat{S}_i - \frac{4}{3}\delta_{ij}\mathbb{1}_3$ [16]. The expectation value of the quadrupole operatos can be intuitively thought of in different ways, one being that they are linked to the second moment of the spin, i.e. fluctuations of a state. The polar state $|\psi_p\rangle = |0\rangle$

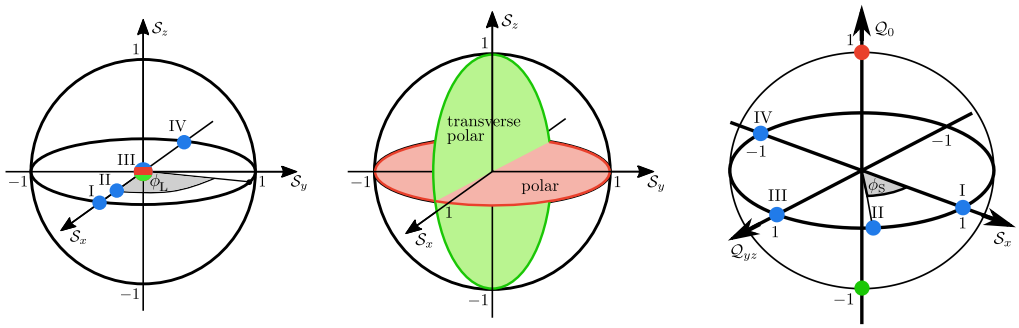

Figure 1: Graphical representation of spin 1 states. Left: Spin sphere, with the expectation values S_x, S_y and S_z on the axes. The Larmor phase determines the orientation of the spin state on the equator of the spin-sphere. Different states are shown, polar (red) and transverse polar (green) state, are indistinguishable due to identical (zero) expectation value for all three observables. Middle: To distinguish polar and transverse polar state, an ellipsoid centered around their expectation value is used to indicate their fluctuations. Right: The spin–nematic sphere allows a visual differentiation between all states shown on the left. Polar and transverse polar state differ in Q_0. The blue dots lie on the equator and differ in their spinor phase, rotating a state around Q_0 and determining the position of a state on the spin–nematic sphere. Figure taken and adapted from [16].

and the transverse polar state $|\psi_{tp}\rangle = \frac{1}{\sqrt{2}}(|1\rangle + |-1\rangle)$ for example have the same expectation value of the spin operators $\langle \hat{S}_i \rangle = \langle \psi | \hat{S}_i | \psi \rangle = 0$, but differ in their expectation value of the operator $\hat{Q}_{zz}$ which is maximal for the transverse polar state and zero for the polar state. This can be implemented in the graphical representation on the spin sphere using not only a point, but also an ellipsoid describing the direction and amplitude of the fluctuations along a given axis on the spin sphere for a potential measurement along that axis (see Fig. 1, middle).

Alternatively, one can introduce another sphere, the so-called spin–nematic sphere (see Fig. 1, right). It is, as the spin sphere, an SU(2) subspace and is spanned by the operators $\{\hat{S}_\perp(\Phi_L), \hat{Q}_\perp(\Phi_L), \hat{Q}_0\}$. These operators are defined via

$$\hat{S}_\perp(\phi_L) = \cos(\phi_L)\hat{S}_x + \sin(\phi_L)\hat{S}_y \tag{3}$$

$$\hat{Q}_\perp(\phi_L) = \cos(\phi_L)\hat{Q}_{yz} - \sin(\phi_L)\hat{Q}_{xz} \tag{4}$$

$$\hat{Q}_0 = -\frac{1}{3}\mathbb{1}_3 - \hat{Q}_{zz} = \begin{pmatrix} -1 & 0 & 0 \\ 0 & 1 & 0 \\ 0 & 0 & -1 \end{pmatrix}. \tag{5}$$

In contrast to the three spin operators, the above mentioned operators do not generally fulfill the SU(2) commutation relations, so that rotations around $\hat{S}_\perp$ and $\hat{Q}_\perp$ do not generally lie on the spin–nematic sphere. They only do under the assumption that $r_1 = r_{-1}$, meaning equal probabilities for states $|\pm 1\rangle$, and for one specific Larmor phase. The exact commutation relations can be found in [16]. However, the operator $\hat{Q}_0$ is the generator of rotations on this sphere and analogously to the operator $\hat{S}_z$ that generates a rotation on the spin sphere and is associated with a propagation of the Larmor phase, the operator $\hat{Q}_0$ rotates a spin into a corresponding quadrupole, which is done via a propagation of the spinor phase. As already

discussed in the example of the polar and transverse polar state, $\hat{Q}_{zz}$ is associated with what will be called the "side mode population" and the shift in eq. (5) is just to center the spectrum around zero. Adding the identity matrix does not change the unitary evolution on the spin-nematic sphere induced by a rotation around the corresponding axis.

2.2 Mean–field description and GPE

The Bose–Einstein condensate (BEC) in our experiment contains on the order of 10^5 spin–1 particles. The mathematical object that describes the three dimensional spin–1 BEC is a three component quantum spin operator field

$$\hat{\boldsymbol{\Psi}}(\boldsymbol{x},t) = \begin{pmatrix} \hat{\Psi}_1(\boldsymbol{x},t) \\ \hat{\Psi}_0(\boldsymbol{x},t) \\ \hat{\Psi}_{-1}(\boldsymbol{x},t) \end{pmatrix}. \tag{6}$$

The individual components themselves are bosonic field operators corresponding to the three m_f sublevels of the system. All phenomena discussed in this thesis can be analyzed on a mean–field level. Therefore, the full quantum operator is replaced by its expectation value

$$\boldsymbol{\psi}(\boldsymbol{x},t) = \langle \hat{\boldsymbol{\Psi}}(\boldsymbol{x},t) \rangle = \begin{pmatrix} \sqrt{n_1}(\boldsymbol{x},t)e^{i\varphi_1(\boldsymbol{x},t)} \\ \sqrt{n_0}(\boldsymbol{x},t)e^{i\varphi_0(\boldsymbol{x},t)} \\ \sqrt{n_{-1}}(\boldsymbol{x},t)e^{i\varphi_{-1}(\boldsymbol{x},t)} \end{pmatrix}. \tag{7}$$

The many particle state is thereby represented by a three component complex valued function, describing the density n_m and the phase φ_m of three magnetic sublevels, respectively. The mean–field approximation can be a valid approximation, but it neglects quantum fluctuations and entanglement. Therefore, it allows to classically simulate the dynamics of a many particle system, and offers a mathematical less involved description than the operator language of the second quantization formalism. The mean field energy is described by

$$E[\boldsymbol{\psi}] = \int d\boldsymbol{x} \left\{ \boldsymbol{\psi}^*(\boldsymbol{x},t) H_0 \boldsymbol{\psi}(\boldsymbol{x},t) + \frac{1}{2} c_0 n^2(\boldsymbol{x},t) + \frac{1}{2} c_1 |\boldsymbol{F}|^2(\boldsymbol{x},t) \right\}, \tag{8}$$

$$\text{with} \quad H_0 = -\frac{\hbar}{2M}\nabla^2 + V(\boldsymbol{x}) - q_{\text{eff}} f_z^2, \tag{9}$$

where H_0 is the non–interacting part of the Hamiltonian. The first term describes the kinetic energy, consisting of reduced Planck constant $\hbar$, gradient ∇, and mass M of the particles. V(x) is the trapping potential, and q_{eff} denotes the second–order Zeeman effect, i.e. an energetic offset of the $m_f = 0$ component with respect to the side modes $m_f = \pm 1$. The first–order Zeeman effect $\sim p f_z$, with p being the energy splitting between the three m_f sublevels due to the magnetic field, is not represented since it can be transformed away by describing the system in a rotating frame with the Larmor frequency. The coupling constant c_0 describes the density-density interaction and c_1 the spin-spin interaction, with $|c_0| \approx 200|c_1|$. This implies that the energy scales associated with the dynamics of the total density are considerably larger than those associated with the spin. The interactions also give rise to two main length scales that govern the dynamics of the system: the density

healing length $\xi_d \sim 0.3\mu$m, and the spin healing length $\xi_s \sim 5\mu$m [17]. The number density n is defined as $n(\boldsymbol{x},t) = \boldsymbol{\psi}^*(\boldsymbol{x},t)\boldsymbol{\psi}(\boldsymbol{x},t)$ and the spin density $\boldsymbol{F}$ is given as

$$F_\nu(\boldsymbol{x},t) = \sum_{m,m'=-1}^{1} \psi_m^*(\boldsymbol{x},t) \cdot (f_\nu)_{mm'} \cdot \psi_{m'}(\boldsymbol{x},t), \tag{10}$$

with the vector f containing the three spin 1 matrices in their three dimensional representation $\boldsymbol{f} = (f_x, f_y, f_z) = (\hat{S}_x, \hat{S}_y, \hat{S}_z)$ as introduced in the previous section. The single components of $\boldsymbol{F}$ are

$$F_x = \frac{1}{\sqrt{2}}\big[\psi_0^*(\psi_1 + \psi_{-1}) + c.c.\big], \tag{11}$$

$$F_y = \frac{i}{\sqrt{2}}\big[\psi_0^*(\psi_1 - \psi_{-1}) + c.c.\big], \tag{12}$$

$$F_z = |\psi_1|^2 - |\psi_{-1}|^2. \tag{13}$$

The complex valued transverse spin $F_\perp = F_x + iF_y$ is defined as

$$F_\perp = \sqrt{2}\big(\psi_1^*\psi_0 + \psi_0^*\psi_{-1}\big) = |F_\perp| e^{i\phi_L}, \tag{14}$$

with the Larmor phase ϕ_L describing the spin orientation in the F_xF_y–plane. For a state on the equator of the spin–nematic sphere ($n_1 = n_{-1} = 0.5n_0 = 0.25n$) the transversal spin length $|F_\perp|$ is given as

$$|F_\perp| = n|\cos\phi_S|. \tag{15}$$

Of special interest are the second–order Zeeman effect q and the spin interaction c_1, since they introduce two competing energy scales that will lead to different magnetic phases of the system. Applying the variational principle to eq. 8, one obtains the classical equation of motion, the Gross Pitaevski Equation or short GPE. It is describing the time evolution of $\boldsymbol{\psi}$, also referred to as the order parameter of the BEC.

$$i\hbar\partial_t\boldsymbol{\psi}(x,t) = \left[-\frac{\hbar}{2M}\nabla^2 + V(\boldsymbol{x}) + q_{\text{eff}}f_z^2 + \frac{1}{2}c_0 n(\boldsymbol{x},t) + \frac{1}{2}c_1 F(\boldsymbol{x},t) f\right]\boldsymbol{\psi}(\boldsymbol{x},t) \tag{16}$$

In the experimental setup, the density distribution can be to some degree described in a Thomas–Fermi approximation [17]. The transversal extent of the density profile is much smaller than ξ_s so that the system can be regarded as quasi–1d in the spin degree of freedom. A quasi–1d GPE can be formulated using modified effective 1d interaction constants $c_{0,1}^{1d}$ and densities n^{1d} [17–19]. The superscript "1d" will be omitted in the following and the 1d description is applied implicitly.

2.3 Mean–field dynamics in the single–mode approximation

A first step towards understanding the dynamics of a 1d spinor BEC can be to focus on the spin dynamics, and assuming that all spin components share the same spatial dependence and only the spin components vary in time. This is called the "Single-Mode Approximation" (SMA), and it is valid, as long as the system size is much smaller than ξ_s. However, when the system size is larger than ξ_s, the SMA

can be applied locally within the local density approximation (LDA) [15]. The aforementioned assumptions can be formulated as follows:

$$\psi_m(x,t) = \sqrt{N}\xi_m(t)\psi_{\text{SMA}}(r)e^{-i\mu t/\hbar}, \tag{17}$$

with a normalized, space–independent spinor $\boldsymbol{\xi}$. The single–mode wavefunction ψ_{SMA} gives the spatial extent of the cloud, and μ is the chemical potential. Plugging this into the GPE (16) yields the equations of motion (EOM) for the single components [14]

$$i\hbar\dot{\xi}_{\pm1} = q_{\text{eff}}\xi_{\pm1} + \tilde{c}_1[\rho_{\pm1} + \rho_0 - \rho_{\mp1} + \xi_0^2\xi_{\mp1}^*] \tag{18}$$

$$i\hbar\dot{\xi}_0 = \tilde{c}_1[(\rho_1 + \rho_{-1})\xi_0 + 2\xi_1\xi_{-1}\xi_0^*] \tag{19}$$

with $\tilde{c}_1 = (N/V^{\text{eff}})c_1 = n_{\text{eff}}c_1$ in the SMA with total atom number N and effective volume $V^{\text{eff}} = (\int dr|\Psi_{\text{SMA}}|^4)^{-1}$ of the system. n_{eff} is a resulting effective density, and $\rho_m \equiv |\xi_m|^2$.

A more intuitive way to visualize the spin dynamics is to look at the mean–field energy functional (see eq. 8). It features only two terms that describe the internal spin dynamics of the system. Expressing these in terms of the spin-1 operators as introduced in section 2.1, allows to express the spin mixing Hamiltonian

$$\hat{H}_{spin} = q_{\text{eff}}\hat{S}_z^2 + \frac{1}{2}\tilde{c}_1(\hat{S}_x^2 + \hat{S}_y^2 + \hat{S}_z^2). \tag{20}$$

Note that c_1 is also here replaced by $\tilde{c}_1$.

Rewriting equation (20) allows a very illustrative picture of the spin interaction dynamics on the spin nematic sphere. Expressing S_z^2 in terms of $\hat{Q}_0$ yields

$$\hat{Q}_0 = \begin{pmatrix} -1 & 0 & 0 \\ 0 & 1 & 0 \\ 0 & 0 & -1 \end{pmatrix} \text{ and } \hat{S}_z^2 = \begin{pmatrix} 1 & 0 & 0 \\ 0 & 0 & 0 \\ 0 & 0 & 1 \end{pmatrix} = -\frac{1}{2}\hat{Q}_0 + \frac{1}{2}\mathbb{1}_3, \tag{21}$$

where the addition of $\frac{1}{2}\mathbb{1}_3$ just induces a constant energy offset and can thus be ignored. Further, if one assumes $\langle\hat{S}_z\rangle = 0$, and without loss of generality chooses ϕ_L to be 0, equation (20) can be rewritten as

$$\hat{H}_{spin}/h = -\frac{1}{2}q_{\text{eff}}\,\hat{Q}_0 + \frac{1}{2}\tilde{c}_1\hat{S}_x^2. \tag{22}$$

This Hamiltonian can be intuitively understood if one looks at the spin–nematic sphere. The first term causes a rotation around the $\hat{Q}_0$- axis, with a frequency independent of the expectation value of $\hat{Q}_0$. The second term is inducing a sheering, i.e. a rotation around the $\hat{S}_x$ axis, with an orientation depending on the sign of $\langle\hat{S}_x\rangle$, and a frequency depending of the amplitude. Because spin mixing conserves the magnetization in z–direction and the Larmor phase, the state has to stay on the surface of the spin–nematic sphere. For large q_{eff}, the first term dominates, and the polar state is stationary. An elongated spin would rotate around the Q_0-axis due to the large second–order zeemann shift. In the other extremal case, where q_{eff} is approximately zero, the polar state is unstable, whereas an elongated spin would be stable. In between those two cases there is a "trapped region" with a stable point, and an "untrapped" or "free–running" region, where the spinor phase

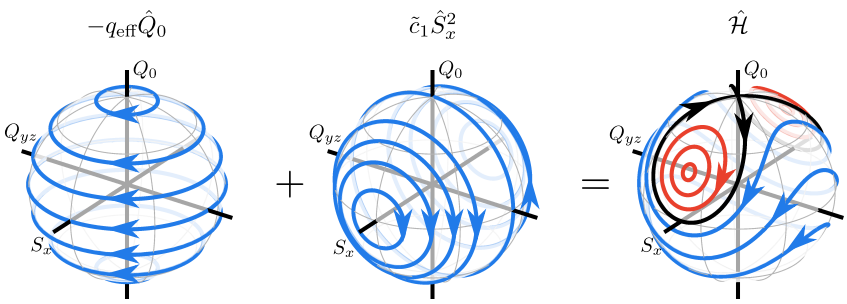

Figure 2: Mean–field nynamics on the spin–nematic sphere. The two terms in the spin mixing hamiltonian (22) lead to a rotation around $Q0$ (left), and a sheering around $\hat{S}_x$ (middle). This results in the formation of a seperatrix (right). For large q_{eff}, the phase space looks like the left panel. As q_{eff} gets smaller, at $q_{\text{eff}} = -2\tilde{c}_1$ ($\tilde{c}_1$ is negative), the seperatrix emerges at the north pole of the sphere. At $q_{\text{eff}} = 0$, it touches the south pole, while the stable point lies on the equator. The right panel shows the phase space for $q_{\text{eff}} = -\tilde{c}_1$. Figure taken from [16].

evolves monotonously. The trajectory that separates the trapped and the free–running region is called "separatrix" (see black line in the right panel of Fig. 2). The position of the stable point can be calculated using the fact that the phase space is spherical ($\sqrt{Q_0^2 + S_x^2 + Q_{yz}^2} = 1$).

$$E_{\text{spin}}/h = -\frac{1}{2}q_{\text{eff}}\,Q_0 + \frac{1}{2}\tilde{c}_1 S_x^2. \tag{23}$$

$$\frac{\partial E_{\text{spin}}}{\partial Q_0} \overset{!}{=} 0 \quad \Rightarrow \quad Q_0^{\text{stable}} = \frac{q_{\text{eff}}}{2|\tilde{c}_1|} \quad \text{and} \quad S_x^{\text{stable}} = \pm\frac{1}{2\tilde{c}_1}\sqrt{4\tilde{c}_1^2 - q_{\text{eff}}^2} \tag{24}$$

As will be presented in Section 5, the 1d system can be uniformly prepared in a state on the equator of the spin–nematic sphere. The dynamics will be locally compared to a simulation of the SMA equation of motion (18) and (19). In general, the SMA is not applicable in the 1d case, since the spin observables can show a strong spatial dependence, so that (17) is not valid. However, since the initial condition is homogeneous in all spin observables, and in the trap center the density only varies on the order of $\sim 10\%$ over $\sim 70\mu$m, it is assumed that the system locally evolves as expected in the SMA, with $\tilde{c}_1 = n_{\text{local}}c_1$. Here n_{local} is the local density and thus this is called a local density approximation (LDA). In the LDA, SMA arguments remain valid in any infinitesimal volume element, and neighbouring volume elements are independent in this limit. [15] [20]. It is expected to be a good approximation, as long as any spatial structure is much larger than ξ_s. This condition is in met in the experiments of Section 5, as one can see in the data.

The simulation yields the trajectory on the spin–nematic sphere for a given initial condition as a function of time. The shape of the phase space only depends on the ratio $q/\tilde{c}_1$ (see fig 2), whereas the "speed" in which a state travels on its trajectory is given by their absolute value. Fig. 3 shows the results for different ratios of q_{eff} and nc_1, and different initial conditions for the Spinor Phase $\phi_{s,\text{initial}}$. The expectation value of Q_0 is obtained via $Q_0(t) = \langle\boldsymbol{\xi}(t)|\hat{Q}_0|\boldsymbol{\xi}(t)\rangle$. The frequency of the oscillation is obtained via a sine fit, the amplitude of the oscillations is obtained as half difference of maximal and minimal value, and the offset is the maximal value

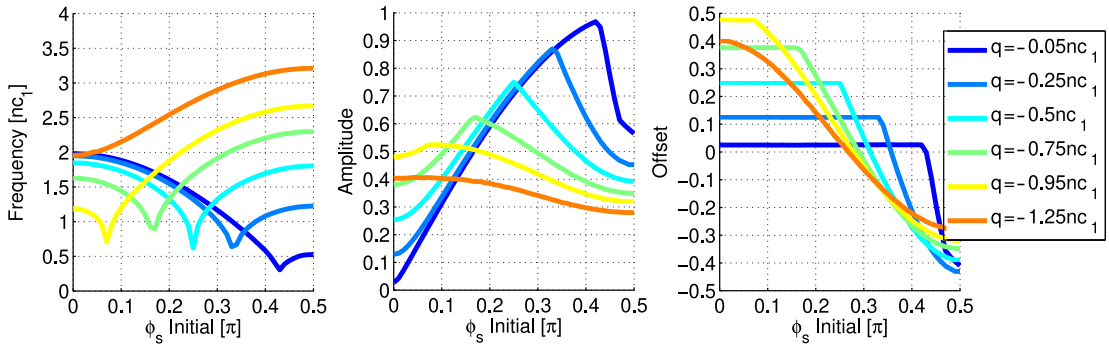

Figure 3: Mean–field dynamics of Q_0 in the single–mode approximation. Shown are the frequency (left), amplitude (middle) and offset (right) of a simulation of $Q_0(t) = \langle \boldsymbol{\xi}(t)|\hat{Q}_0|\boldsymbol{\xi}(t)\rangle$ using eq. (18) and (19). A sine fit used to extract the frequency. It is given in units on nc_1, corresponding to $\tilde{c}_1$ in (18) and (19). The colors indicate different ratios of q_{eff} (referred to as "q" ind the label on the right), and $\tilde{c}_1$. Each color thus represents one shape of the spin–nematic phase space, characterized by a set of trajectories (see Fig. 2). On the x axis, the spinor phase initial condition is plotted. Thus every point on a graph belongs to a different trajectory, characterized by its amplitude, offset and frequency in Q_0. The dip in the frequency is where the initial condition crosses the separatrix, and the frequency goes to zero (not visible due to sampling of $\phi_{s,\text{initial}}$). On the left of the dip, the state moves on a trapped trajectory, while on the right it is free running. To interpret the graphs shown here, Fig. 2 can be of great help. For example the dark blue line represents trajectories for a small q_{eff}, where $\tilde{c}_1$ dominates and the phase space looks almost like the middle panel in Fig. 2. This can be nicely validated, by looking at the amplitude, which is almost zero for an initial $\phi_s = 0$ (middle). It increases as expected with increasing initial ϕ_s, while the offset (right) remains zero. The frequency (left) goes down for increasing initial ϕ_s. This can not be seen by looking solely at Fig. 2. The knowledge of the frequency for all trajectories with a given ratio of q_{eff} and $\tilde{c}_1$ is the main purpose of the simulation. Note that for trapped oscillations, the offset is independent of the initial condition as the stable point is a property of the phase space (24). This will be used in section 5, to determine q_{eff}/nc_1 via eq. 24.

minus the amplitude. The analytical solution of $Q_0(t)$ can be expressed in terms of elliptical sine functions [14]. Performing an exact fit of these to the simulation however turned out do be very involved. The quality of the sine fit depends strongly on the trajectory and especially fails close to the separatrix. It is therefore only used to obtain the frequency, with a very precise previous estimation and small tolerances, calculated from the temporal distance between maxima and minima of the function. With this method, the frequency is obtained precisely and the fit quality can be validated. The right panel of Fig 2 helps to understand the simulation results resented in Fig. 3. A further insight into the simulation is given in the Appendix A.

2.4 Phase diagram and post quench dynamics

This Subsection, being the last part of the theoretical background, is meant to give a short introduction into experiments that were performed in this group, where

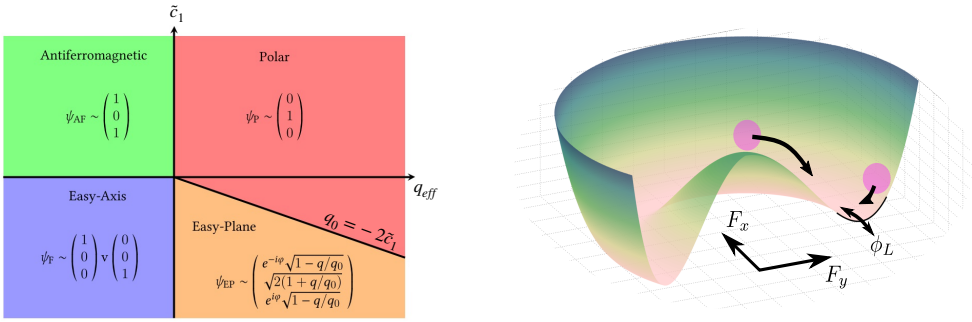

Figure 4: Left: Mean–field phase diagram in the q_{eff}–$\tilde{c}_1$ plane. Right: Mean–field energy potential in the easy–plane phase. The polar state at the center is unstable, the ground state is characterized by a non–vanishing spin length and a Larmor phase. Note that this representation is connected to the spin–mixing dynamics on the spin nematic sphere (see Fig. 2), where the rim represents the stable point in S_x. This visualization emphasises that the ground state is characterized by a certain spin length, independent on the orientation. This potential does not show, however, that the transversal spin length can be reduced in two ways (without rotating the vector into F_z), namely by changing the spinor phase, or the side mode population, which is seen better in the representation on the spin–nematic sphere.

universal dynamics far from equilibrium was observed [12]. A recent paper has linked this dynamical behavior to vortices in the transverse spin $F_\perp$ in space and time [13]. These vortices are associated with a dip in the spin length $F_\perp$, and aa 2π–winding of the spin orientation, that is, the Larmor phase ϕ_L on a closed curve around that dip in space and time. Therefore, they will also be referred to as vortices in the Larmor phase. Developing a scheme for the deterministic preparation of such a vortex was the main motivation for the work of this thesis.

The parameters q_{eff} and $\tilde{c}_1$ span a phase diagram, which is depicted in Fig. 4 (left). The different phases are associated with different mean–field ground states. In the experimental setup, c_1 has a fixed negative value due to the ferromagnetic interaction of ^{87}Rb and cannot be changed. With control over q_{eff}, the system can be prepared in three different magnetic phases: the polar, the easy–plane, and the easy–axis phase. A sudden change of q_{eff} is referred to as "parameter–quench".

Of special interest is the second–order quantum phase transition from the polar to the easy–plane phase. Starting in the ground state of the polar phase (polar state, with zero magnetization), quenching into the easy–plane drives the system to a far–from–equilibrium state in the new Hamiltonian. The easy–plane ground state is a state in the F_xF_y–plane with a non–zero spin length, thus the order parameter in this phase is the transversal spin $F_\perp = F_x + iF_y$, and the phase transition breaks the SO(2) symmetry of the polar phase.

The initial dynamics in an elongated system after a parameter quench can be described by the Bogoliubov approximation, that predicts the growth of certain momentum modes in the transversal spin [11]. Nonlinear interactions lead to the formation of spin domains, setting the stage for the subsequent ordering process. After some time, the subsequent dynamics show a self–similar scaling behavior of the structure factor $S(k,t) = \langle |F_\perp(k,t)| \rangle$, associated with the proximity to a non–thermal fixed point. $\langle ... \rangle$ denoting the average over different runs. The self–similar

scaling has been extensively studied in theory [7, 11, 21], and has been observed for the first time in this experiment in 2018 [12]. A numerical study has linked universal dynamics in the quenched spinor BEC to rogue–wave like events in the single magnetic components, resulting in real–time instanton defects, that appear in the Larmor phase as vortices in space and time [13]. Taken from that work, Fig. 5 shows an excerptn of a single run of the simulated space–time evolution after a quench. Instantons are associated with a change in the winding number

$$Q_w = \frac{1}{2\pi} \int_0^L dx \frac{\partial \phi_L}{\partial x} \in \mathbb{Z}, \tag{25}$$

which has to take integer values, since the simulation is performed with periodic boundary conditions.

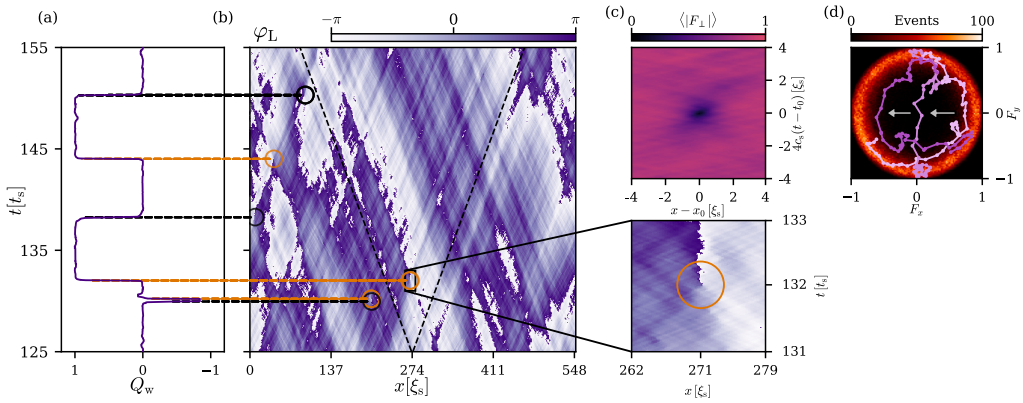

Figure 5: Time evolution of the Larmor phase after a quench (a) time evolution on the winding number Q_w for the run shown in panel (b). (b) spatio–temporal evolution of the Larmor phase in one single run. The dashed line indicates the spin speed of sound. (c) Structure of the real–time instanton. The upper panel shows averaged $F_\perp$ profiles for several defects. The lower panel is a zoom in panel (b) and shows the vortex–like structure of the defect in the Larmor phase, indicated by the orange circle, around which the phase exhibits a 2π–winding. (d) The $F_\perp$ field configuration for three different times (bright to dark pink), in spin space. The outer red circle represents a histogram over 100 runs. The instanton is associated with a local crossing of the center of the $F_x F_y$–plane. There the spin length has to go to zero, and the winding number changes by ± 1, depending on the direction of the traversal.

A comparable excerpt of the post–quench dynamics from experimental data can not be obtained. As a measurement destroys the BEC, each subsequent measurement in a time series can only show the time evolution of a different state at a certain time. Objects like the vortices in the Larmor phase that show up randomly can thus not be observed. Starting from a different initial condition that allows the deterministic preparation of a vortex, however, can in principle be archieved, and poses one goal of this work (see Section 6.3).

3 Experimental system

Following the theoretical introduction to the spin-1 system, the experimental setup will now be presented: A quasi–1d spinor Bose–Einstein condensate of ^{87}Rb, consisting of roughly up to 150k atoms. A typical experimental sequence consists of three stages: state preparation, time evolution, and readout of the final state.

After a sequence of different trapping and cooling stages, the atoms are confined in an elongated optical dipole trap. The trap frequencies are approximately $(\omega_\parallel, \omega_\perp) \approx 2\pi \times (2, 250)$ Hz [16]. The electron spin S = 1/2 and the nuclear spin I = 3/2 couple to two hyperfine spin states F = 1, 2, giving rise to the magnetic sublevels $|F, m_f\rangle$, with $m_f = -F, \ldots, F$ (see Fig. 6, center). The experiments take place in a homogeneous magnetic field ($\sim$ 1G), defining the quantization axis along the z–direction. This leads to an energy shift of the levels in both hyperfine manifolds, given by

$$E_z/h = g_{1,F} m_f B + g_{2,F}(4 - m_f^2)B^2 \tag{26}$$

with the first– and second–order g–factors [16]

$$g_{1,F} = \begin{cases} -700 \text{ kHz/G} & \text{for } F = 1 \\ 702 \text{ kHz/G} & \text{for } F = 2 \end{cases} \text{ and } g_{2,F} = \begin{cases} -72 \text{ Hz/G}^2 & \text{for } F = 1 \\ 72 \text{ Hz/G}^2 & \text{for } F = 2 \end{cases}. \tag{27}$$

The Hamiltonian due to these magnetic field shifts is for the F = 1 manifold given by

$$\hat{H}_B/h = p_B \hat{S}_z + q_B \hat{Q}_0 \tag{28}$$

with $p_B = g_{1,1}B$ and $q_B = g_{2,1}B^2$ being the first– and second–order Zeeman shift, respectively. Thus, the first–order Zeemann effect causes an evolution of the Larmor phase ($\omega_L \approx 2\pi \cdot 700$kHz), and the second–order Zeemann shift leads to an evolution of the spinor phase ($\omega_S \approx 2\pi \cdot 72$kHz).

Global rf and mw control

Within one hyperfine manifold F, the magnetic sublevels can be coupled via rf fields, using two rf–coils. An rf–coil generates an oscillating B field perpendicular to the offset field. In the rotating frame of the atoms, the time evolution of their state is governed by [16]

$$\hat{H}_{\mathrm{B}}^{\mathrm{rot}} = \hbar\Omega_{\mathrm{rf},0}[\cos\phi_{\mathrm{rf}}\hat{S}_y - \sin\phi_{\mathrm{rf}}\hat{S}_x] - \hbar\delta\hat{S}_z \tag{29}$$

with the detuning $\delta = \omega_L - \omega_{\mathrm{rf}}$. A resonant rf–pulse ($\omega_{\mathrm{rf}} = 2\pi p_B$) induces Rabi oscillations with a frequency given by the resonant Rabi frequency $\Omega_{\mathrm{rf},0} = |g_{1,1}|B_{rf}/2$. The rotation axis for a Rabi pulse is defined by the phase of the rf–pulse. The two coils are needed to selectively address the two hyperfine manifolds, which is important for the readout. One of them is also used to compensate/induce gradients of the offset magnetic field.

For coupling between two levels in different hyperfine states, a mw–coil is used (see Fig. 6b). This corresponds to a two-level system, described by the spin–1/2 operators. The selection rules for dipole transitions allow only transitions with $\Delta m_f = \{0, \pm 1\}$. The mw generator is always set to a fixed frequency of 6.8GHz, that corresponds to the hyperfine splitting of the F=1 and F=2 manifold. The signal is fed into an I/Q mixer, the additional inputs of the mixer are rf signals from an AWG to control the phase and frequency of the micro wave. After that, the signal passes

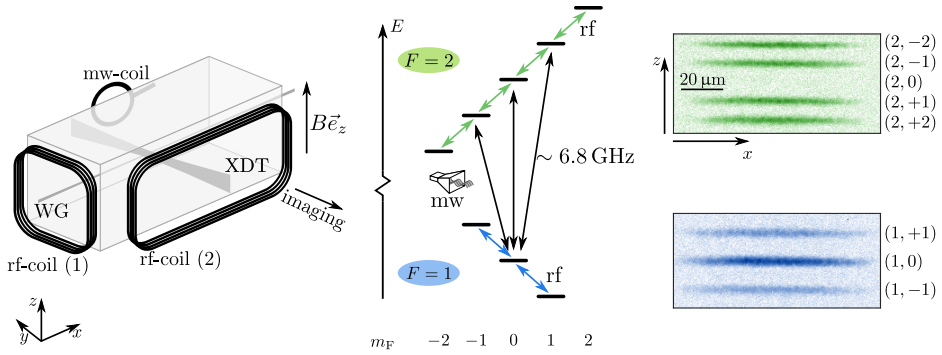

Figure 6: Left: Sketch of the experimental setup. The BEC is confined in a dipole trap within a glass cell. The two dipole lasers are referred to as WG and XDT. For the performed experiments in the 1d system, the XDT is turned off, so that the cloud is extended in the x–direction. Two rf–coils and a mw–coil are employed to control the atoms. Middle: Level–scheme of ^{87}Rb. Inside one hyperfine manifold, rf pulses couple the magnetic sublevels. The mw pulses are used to couple states between the manifolds. Right: Example of an absorption image revealing the densities in the individual sublevels. Figure is adapted from [22].

an electronic switch and an amplifier before it is radiated from the antenna close to the atoms. Short mw pulses that resonantly couple specific magnetic sublevels between the two hyperfine manifolds are used for state preparation and readout. During the time evolution of a state, off–resonant coupling of the two $m_f = 0$ states is used to control the second–order Zeeman shift (see Section 5).

Local control

Additionally to global control via rf and mw fields, also a steerable laser allows for local control. Its timing, position, and intensity is controlled via two acousto-optic deflectors (AODs), for the horizontal and vertical beam position. The setup is discussed in detail in [17]. The off–resonant interaction of the laser light with the atoms is described by the AC–Stark effect, consisting of a scalar and a vector component [23]:

$$\hat{\mathcal{H}}_{\text{Stark}} = -\frac{1}{4}\left(\alpha^s(\boldsymbol{E}_1^* \cdot \boldsymbol{E}_2)\mathbb{1}_3 - \frac{i\alpha^v}{2F}(\boldsymbol{E}_1^* \times \boldsymbol{E}_2)\hat{\boldsymbol{F}}\right), \tag{30}$$

with the light field components $\boldsymbol{E}_j = E_j \boldsymbol{\mathcal{E}}_j e^{i(\omega_j t + \phi_j)}$, scalar and vector polarizabilities α^s and α^v, and Spin Operator $\hat{\boldsymbol{F}}$. Making use of the vector Stark shift, the local laser is able to create a fictitious magnetic field in beam direction, given as [17]

$$\boldsymbol{B}^{\text{fict}} = \frac{i\alpha^v}{8 g_F \mu_B F}\boldsymbol{E}_1^* \times \boldsymbol{E}_2. \tag{31}$$

The first term in (30) gives rise to the scalar Stark shift which is describing the dipole force that is e.g. used for the dipole trap. Since the polarizabilities α include transition matrix elements of the atoms, they depend on the detuning of the laser light with respect to the possible atomic transitions. The dipole force is attractive for red, and repulsive for blue detuned laser light. For a wavelength of $\sim$ 790.081nm,

between the D_1 and D_2 absorption lines, the scalar shifts due to the two transitions cancel out for the F = 1 manifold. The tune–out for the F = 2 manifold lies at $\sim$ 790.032nm [24–26]. This difference is however small enough to be negligible for the cases discussed here. This wavelength is chosen for the local beam to create local spinor phase rotations (see Section 4 for details).

Readout

The readout allows the measurement of non–commuting spin observables by using the F=2 manifold. Note, that the physics of interest are confined to F=1 and F=2 thereby is only used in terms of preperation and readout sequences. The readout is in detail discussed in [16, 22]. First, global spin rotations are used to map the desired observables to the measurable occupation numbers of the hyperfine levels. A magnetic field gradient in z-direction is then applied (Stern–Gerlach pulse) to spatially separate the magnetic sublevels. Followed by a short time of flight ($\sim$ 2ms) the populations in the sublevels are then measured via high–intensity absorption imaging. In this work, a dual readout of F_x and F_y is used to obtain the complex valued transverse spin $F_\perp = F_x + iF_y$. Note that with $F_\perp = |F_\perp| \cdot e^{i\phi_L}$ the readout spatially resolves the Larmor phase, up to a global phase that may differ for different experimental realizations. This is due to fluctuations in the offset magnetic field and becomes relevant for evolution times larger than roughly ($\sim$10ms). In the following, $F_\perp$ is often used interchangeably with its absolute value $|F_\perp|$. In addition, the F_z readout is used to obtain F_z and Q_0. The sequence of the readout and the calculation of the spatially resolved spin observables from the atom numbers in the individual levels is given in [17].

4 Local control of the spinor phase

In the following, the experimental scheme for local spinor phase imprints will be presented. We will then present and discuss calibration measurements that confirm the reliabiltiy of the imprinting technique and point out how to utilize the presented method in order to generate interesting initial conditions.

4.1 Method for local spinor phase rotations

The underlying idea of the local spinor phase imprint is to use the fictitious B-Field of the local laser (see eq. 31 and [17, 27] for details), to create the desired phase imprint in the single m_f components. In an external magnetic field, the single magnetic levels experience a relative phase evolution proportional to their magnetic quantum number m_f and the B–field (neglecting the second–order Zeeman shift, interactions, and a total global phase evolution depending on the chemical potential):

$$\frac{d}{dt}\left(\phi_{F,m_f}(x)\right) \sim m_f g_{1,F} B(x), \quad \text{with} \quad B(x) = |\boldsymbol{B}_{\text{off}} + \boldsymbol{B}_{\text{fict}}(x)| \tag{32}$$

$\boldsymbol{B}_{\text{off}}$ being the offset magnetic field ($\sim$ 1G) and $\boldsymbol{B}_{\text{fict}}(x)$ the perpendicular fictitious field created by the local laser beam at the tune–out wavelength. In the case of a state in the F=1 manifold with non–zero densities in all three m_f sublevels, this would locally lead to the accumulation of a spatially dependent Larmor phase. Locally the Larmor phase $\phi_L(x) = (\phi_1 - \phi_{-1})/2$ has a faster time evolution, thus after a time T_{hold}, a different phase is accumulated than in the rest of the cloud, leading to a local shift of the Larmor phase $\Delta\phi_L(x) \sim B(x)T_{\text{hold}}$, and thus a locally modified spin direction. Adapting this idea to the spinor phase $\phi_S = \phi_0 - (\phi_1 + \phi_{-1})/2$, one can make use of the very similar (but opposite sign) g-factors of the F=1 and

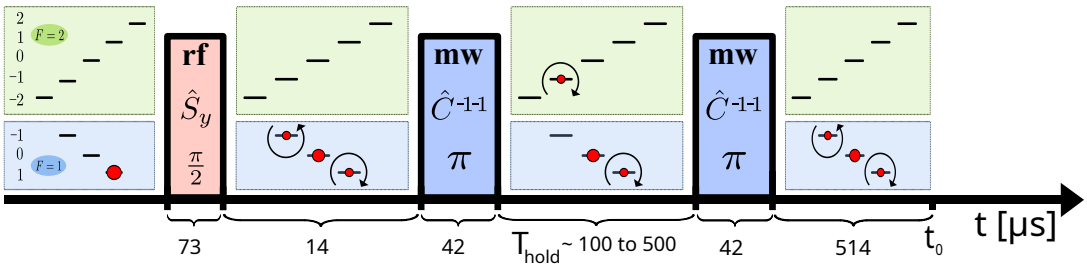

Figure 7: Scheme of the local imprint technique: Initially, only the $|F, m_f\rangle = |1, -1\rangle$ atoms are trapped (left). The two hyperfine manifolds are represented in blue and green, with red dots representing the densities in the individual levels. An rf pulse (red) prepares a state in the F_xF_y–plane. The circular arrows indicate the rotation of the phase with respect to the $m_f = 0$ states. Subsequently, a mw pulse (blue) transfers the atoms from $|1, -1\rangle$ to $|2, -1\rangle$. At this point, the two side modes rotate in phase, with a frequency dependent on the B-field. After the time T_{hold}, the atoms are transferred back with another mw pulse. A spinor phase, represented by the function $\phi_s(x) \sim B(x)$, has been accumulated over this period. At the time t_0, the state preparation is completed, and the time evolution begins. The 514µs following the second microwave pulse are required for the proportional-integral-derivative (PID) controller that regulates the microwave dressing. The layout of this Figure is adapted from [16], and the rf and mw pulses are defined in a similar manner.

F=2 manifold. Transferring the atoms of one F=1 sublevel with $m_f \neq 0$ to the F=2 sublevel with same m_f, during the time T_{hold} (and subsequent back–transfer), allows to obtain a Spinor Phase evolution depending on the B–field, and thus also featuring the local imprint due to the laser beam. The scheme is depicted in Fig. 7. At t_0, the evolution time begins.

Globally, a Spinor Phase Imprint would also work without the time T_{hold} between the two mw pulses. The phase imprint would then just be depending on the relative phase of the two mw pulses. However this method does not allow for a local phase rotation. The imprint method does not change the Larmor phase locally, since for the times T_{hold} considered here, the difference of the g-factors of $\sim 0.3\%$ as well as the second order Zeeman effect are negligible.

Since there is a certain jitter in the position of the beam in both the horizontal and vertical direction, the method of using several pulses in the z-direction was adopted from [27]. Each imprint position on the condensate consists of three subsequent pulses in the z-direction, which turned out to be sufficient. Their positional spacing is $\Delta f_{\text{AOD, V}} = 0.14\text{MHz}$ (given as the vertical AOD frequency). This was found to be the optimal frequency spacing for a homogeneous beam profile in transversal direction in [27] by applying amplitude modulation to the local beam (and thereby inducing a local rf rotation) and imaging the density profile in the S_z readout. Their temporal separation is a buffer time of $\tau_{\text{buff}} = 4.5\mu\text{s}$. It is needed as the sound wave in the AOD of consecutive pulses would otherwise interfere. During the time T_{hold}, several horizontal positions in the cloud can be illuminated consecutively to create the desired imprint shape. The frequency of the horizontal AOD $f_{\text{AOD, H}}$ controls the position with $1\text{MHz} \mathrel{\widehat{=}} (39.5 \pm 0.8)\mu\text{m}$. A schematic of this idea is presented in Fig. 8. T_{hold} then has to be adjusted so that the pulses, including the buffer times, fit into the given time window. The duration of each pulse is given as $\tau_{B,i}$. With each imprint position consisting of three pulses, the condition for T_{hold}

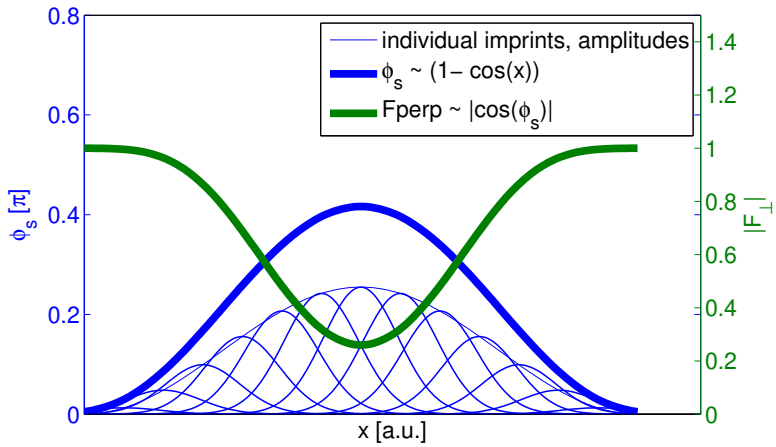

Figure 8: Conceptual scheme for using multiple imprints to create a desired shape in ϕ_S and $F_\perp$ (bold blue and green). Here a cosine–shaped profile is imprinted in the Spinor phase using 13 individual imprint positions (blue). The single imprints are represented by Gaussians in the spinor phase with different amplitudes, separated by roughly 1.5σ. In the experiment, each imprint position is realized by three subsequent laser pulses with the same horizontal position, given by the frequency $f_{\text{AOD, H}}$, and three vertical positions $\{f_{\text{AOD, V}}, f_{\text{AOD, V}} \pm \Delta f_{\text{AOD, V}}\}$.

reads

$$T_{\text{hold}} \overset{!}{>} \sum_{i=1}^{N} 3(\tau_{B,i} + \tau_{\text{buff}}) - \tau_{\text{buff}} \tag{33}$$

for a total imprint imprint using N single imprint positions, and thus requiring in total 3N beam positions. The current experimental setup allows a maximum of 14 beam positions, corresponding to 42 single laser pulses, as the programming of the AWGs for the local control causes problems with more pulses.

4.2 Experimental analysis of the state preparation

First, the effect of changing the time T_{hold} was observed without local laser pulses. The local imprint was then tested with one beam position for different beam times and powers.

4.2.1 Background oscillation

The obtained data are shown in 9a. The data were taken after an evolution time of 5µs with the F_xF_y –readout (see Section3). The $F_\perp$ profile is flat over the whole condensate, with an offset $F_{\perp,\text{BG}}$ depending on T_{hold}. The latter is expected to globally rotate the spinor phase $\phi_{S,\text{BG}} \sim T_{\text{hold}}$, thus with (15), an oscillation is expected for $F_{\perp,\text{BG}}$. However, the observed frequency of $f = (15.9 \pm 0.18)$MHz is much higher than the expected value of $\sim$ 700kHz (which is the Larmor frequency in our external B–field of $\sim$1G, see eq. 28). The explanation is found by looking at the signal of the TTL switch that is controlling the exact timing of the second mw pulse, and the IQ AWG signal that enters an I/Q–mixer with the microwave signal to control the frequency and phase of the mw pulse. The time T_{hold} is set in the script that programs the AWG for the TTL switch as well as the IQ AWG. While the TTL AWG gets all timings rounded to 0.1µs, the IQ AWG gets its timings without rounding. Looking at the AWG signals on an oscilloscope (see 9b), one can see that a change of $\Delta T_{\text{hold}} = 10$ns leaves the TTL unchanged but induces a delay of 10ns of the IQ AWG signal. This causes a phase shift of the second mw pulse and explains the fast oscillation in 9a. The phase of the second mw pulse determines the phase of the $m_f = -1$ sublevel with respect to the other two sublevels and thus affects both Larmor and spinor phase. This is seen in Figure 9a, as both spin length and orientation vary. Recalling the definitions for ϕ_L and phi_S explains that the oscillation in both is just given as half the frequency of the IQ AWG. What was effectively scanned in this experiment was the phase of the two mw pulses, and not the time T_{hold}.

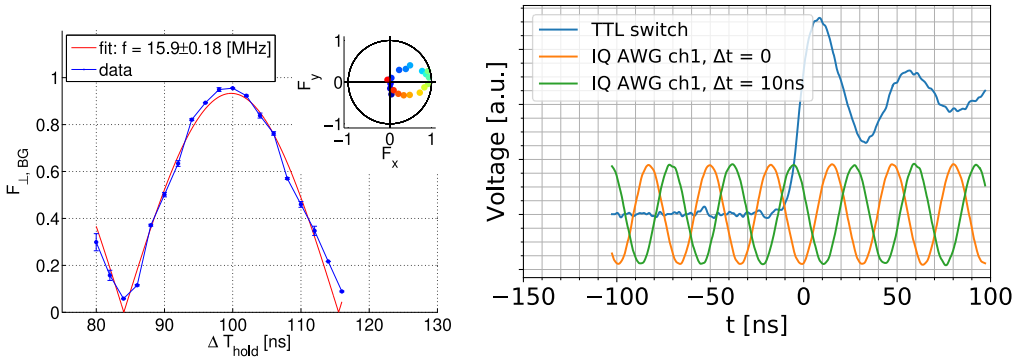

(a) (b)

Figure 9: Left: Spin length (blue) for different values of T_{hold} with $T_{\text{hold}} = 103\mu\text{s} + \Delta\text{Thold}$. Error bars are the square root of the variance of 2 to 4 realizations. This is of course not enough statistics to obtain a meaningful estimation of the actual error, but serves as a first idea of the fluctuations. The fit function (red) is $F_\perp = F_\perp^0 |\cos(2\pi f + \delta)|$ and yields a frequency of $f = (15.90 \pm 0.18)$MHz. The inset shows the spin orientation for different times, indicated by the color. Right: Oscilloscope data of the TTL switch (blue) and the IQ AWG (orange and green) signal on the onset of the second mw pulse in the state preparation. The TTL switch controls the timing of the mw pulses. The IQ AWG is used to modify frequency and phase of the mw pulses, and is added to the mw output in an I/Q–mixer. One can see, that for two different timings Δt (defined as in fig 9a) the TTL switch does not change, but the phase of the AWG output. This explains the fast oscillation in the left figure. The frequency f corresponds to half the frequency of the signals in the AWG output.

4.2.2 Analysis of shape and depth of the local imprint

The initial condition (5µs evolution time) in $F_\perp$ was measured for different local imprints. Beam times τ_B between 0 and 20 µs were chosen for AOD powers between 0.7 and 1.5 Volts. The power is given in units of Volts, as it is set in the control system of the experiment as the amplitude for the AWG signal that controls one of the AODs for local control, while the other one is always set to 1.6V. As mentioned above, the imprint consists of three consecutive pulses with different y–positions. τ_B refers to the duration of each of these pulses. All measurements were performed with the same T_{hold} of 103.1µs, where the background spin length is expected to be maximal (see Fig. 9a). The imprint position was chosen to be very far to the right of the condensate, since otherwise the imaging of such short evolution times interfered with stray light of the local imprint. This effect was experimentally found to be small for beam positions with vertical AOD frequencies $f_{\text{AOD, vert.}} < 97.6$Mhz.

Examples of the imprint shape are shown in figure 10 (upper panel), together with the fit function that was used to determine the depth and width of the imprint. The fit function is

$$F_\perp(x) = F_{\perp,0}\left|\cos\phi_s(x)\right|, \quad \text{with} \quad \phi_s(x) = \phi_s^{x_0} \cdot e^{-\frac{(x-x_0)^2}{2\sigma_B^2}} + \phi_{s,BG}, \tag{34}$$

and shows a very good agreement with the data. $F_{\perp,0}$ respects, that even a fully elongated spin ($\phi_S = 0$) does not necessarily lead to a measured value of $F_\perp = 1$

(see e.g. Fig. 9a). $\phi_s^{x_0}$ is the relative spinor phase at the center x_0 of the imprint with respect to the background Spinor Phase $\phi_{s,BG}$. Assuming a Gaussian shape in the spinor phase, σ_B describes the width of the imprint.

The fit was applied to single realizations (~ 20 per setting) and thus quite noisy data. Especially for smaller imprints, the noise is more relevant, and thus the fit function uses the many free parameters ($F_{\perp,0}, \phi_s(x_0), x_0$ and σ_B) to fit the curve to the noise. The lower left panel of figure 10 is the histogram of the imprint widths obtained from single fits, showing values of $\sigma_B = (5.7 \pm 0.7)$µm. The many occurrences on the left edge of the fit range ($\sim (4.9 - 6.5)$µm) are mainly due to small imprints, where the noise is dominant. Also, the imprint was made on an elongated spin ($\phi_s \approx 0$), so that very small imprints are invisible in $F_\perp$ anyway (see, e.g., eq. 34). The peak on the right stems from strong imprints, where the upper limit of the fit range was mandatory since otherwise the fit converged to a wrong shape, not featuring the sharp structure at the imprint center (see upper right in Fig. 10). In general, an increase of σ_B was observed with the imprint strength, but was not significant with respect to the fit errors (given as the 1σ confidence interval of the fit). This might be due to a non–Gaussianity of the imprint that is compensated, and most likely also due to density effects (see below). The position of the imprint is shown in the lower middle panel of Fig. 10. It shows roughly a Gaussian distribution with a standard deviation of 0.7µm, which is approximately

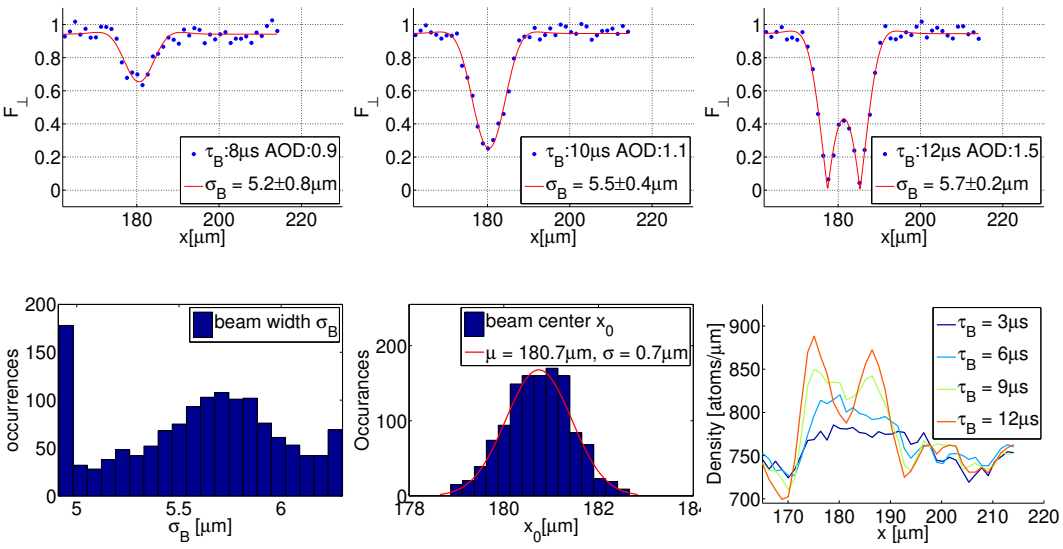

Figure 10: Upper panels: different examples of the spatial $F_\perp$ profile. The blue dots are the data of one single realization representing three binned pixels. The red curve is a fit function, assuming a Gaussian imprint in the spinor phase (see eq. (34)). Labels give the time and power of the local beam, as well as the width obtained from the fit for the shown realization. Lower panels: (left) histogram of the fit result for the beam width σ_B. (middle) histogram of the fit result for the beam position x_0. A gaussian fit yields a jitter of 0.7µm. (right) the total density exemplary for the strongest AOD power (1.5V). An overdensity is created for increasing beam times. For very strong and sharp overdensities (long beam times), the time to the imaging of $\sim$ 2ms is enough to let the peak split. For lower powers, only the overdensity, and not the splitting is ovserved.

$0.1\sigma_B$.

Figure 11 (left) shows the dependence of the imprint depth on the beam time for different beam powers (controlled by the AOD). For all AOD powers and most beam times, an error in the imprint depth of roughly $\Delta\phi_s^{x_0} \approx 0.1\pi$ is observed. This might be due to actual fluctuations in the imprint depth, but can also be due to the problematic choice of the elongated background spin. To disentangle the two effects, it would be beneficial to repeat the measurement at a different background spin length. Due to better visibility, only three of eight measured AOD powers are shown in the plot. In the most simple case, one would expect a linear increase of $\phi_s(x_0)$ with τ_B. However, three more effects are visible here: A concavity down/damping for long times as well as deep imprints, and a concavity up for very short times, which is mostly visible for the strong powers. The concavity up of the curve for small times τ_B can be understood as the fit is very sensitive to the noise for small imprints and seems to overestimate the imprint depth systematically. Also, the sound wave in the AOD needs some time to build up. For AOD powers below 0.9, the spinor phase cannot be rotated more than 0.5π due to the damping effect, while for the largest power, the curve appears to get some damping after $\sim$ 10µs. Both damping effects might have to do with density effects. The total density for the strongest AOD power is shown in the lower right panel of Fig. 10. Since the tune-out wavelength (see Section 3) might not be perfectly matched, the scalar stark effect does not vanish, and the local imprint laser creates an attractive potential. This leads to atoms with the background spinor phase to flow to the beam center, so that the imprint is effectively weakened. For small powers, it might also be useful to remember that the offset B–field and the fictitious B–field are perpendicular, so that they add squared and not linearly. For very strong imprints, the over density is so large that the short time to the imaging of a few µs is enough for the local wave packet to disperse and split into two packets propagating outwards. This is only achieved for the large powers that create a sufficiently strong dipole potential and can thus only explain the damping for very strong imprints. The given explanation of the density effects is still somewhat speculative, and can be tested by for example scanning the wavelength of the local laser.

Despite the previously discussed deviation from the expected linearity, a linear fit was performed to a hand–picked linear regime of the curves in the left panel of Fig. 11. Thus one has to be careful interpreting these data. The result is shown on the right in the Fig. 11. As expected, one can see an increasing slope (upper right). The exact functional shape depends on the diffraction efficiency of the AOD and the quadratic addition of the offset and fictitious B–field. The lower right panel shows the x–intercept of the fit. It lies at $\sim$ 2.5µs for the larger powers, and significantly lower for small powers. This is because the small powers show almost no linear regime (see the blue curve in Fig. 11, left), and thus are not suitable for this fitting method. The x–intercept is interpreted as the time that is needed for the sound wave in the AOD to build up. The AOD size and sound velocity give timings on the order of a few µs. This is also why in between two pulses, a buffer time is needed, as already mentioned in [27]. To improve this measurement, it has to be repeated with a different background spinor phase, that is, a different T_{Hold}, to obtain a better signal for small imprints. Also, the local imprint laser wavelength might have to be changed to better match the tune–out wavelength.

The main results of this analysis are that the Gaussian in the spinor phase

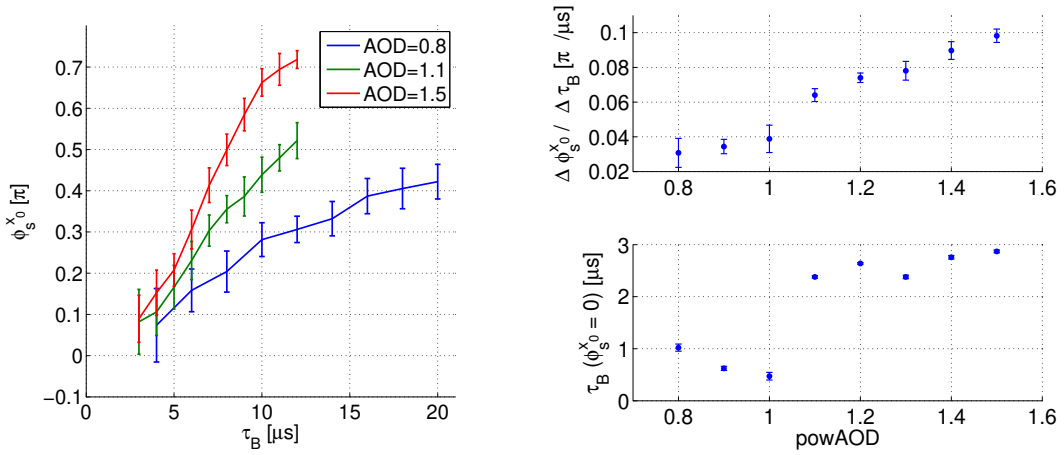

Figure 11: Left: The fit result for the Spinor Phase at the center of the imprint $\phi_s^{x_0}$ is plotted against the beam times for different AOD powers. For each setting, the fit is performed for ~ 20 realizations, the error bars are the standard deviation of the fit result. Right: A linear fit is applied to a hand–picked linear regime in the left plot. The slope (top) and the x–intercept (bottom) are plotted against the AOD power.

describes the imprint well, with a width of (5.7 ± 0.5)µm. To create an imprint, times larger than $\tau_B \approx 2.5$µs have to be used. Density effects may lead to a damping of the imprint. For low AOD powers (< 1V) this damping prevents imprints deeper than 0.5π, while for large powers, the damping becomes relevant for imprints deeper than 0.6π. The positional jitter of the imprint is 0.7µm.

5 Global spin dynamics

The dynamics of homogeneously prepared spin profiles is studied for different second–order Zeemann shifts q_{eff}. After presenting the experimental method for the control of q_{eff}, the results of the experiments are analyzed and discussed.

5.1 Control of the second–order Zeemann shift

After a desired initial condition is prepared, usually a time evolution under a given Hamiltonian is of interest. The two contributing parts in the spin mixing Hamiltonian are the spin-spin interaction $\sim \tilde{c}_1$ and the second–order Zeeman shift $\sim q_{\text{eff}}$ (see ([20])). The value of $q_{\text{eff}}/\tilde{c}_1$ determines the position in the phase diagram (see Fig. 4), and thus the ground state and the overall shape of the phase space (see Fig. 2). The microscopic process behind this interplay is the mechanism of spin–changing collisions (SCC) (see Fig. 12). The density independent spin interaction constant c_1 is a property of the ^{87}Rb atoms and has a fixed negative value (ferromagnetic interaction). The effective value q_{eff} is shifted by dressing the system with microwave radiation and thus tuning the SCC to resonance [16]:

$$q_{\text{eff}} = q_B + q_{\text{mw}} \quad \text{with } q_{\text{mw}} = \frac{\Omega^2}{2\pi 4\delta_{\text{mw}}}, \tag{35}$$

where q_B is a property of ^{87}Rb and applied offset B–field (see eq. 28) and q_{mw} is the shift due to the dressing. The resonant Rabi frequency Ω depends on the field strength of the mw radiation and the detuning δ_{mw} to the atomic transition. Since Ω is not known exactly and fluctuates, the value of q_{eff} has to be measured experimentally and is crucial for a comparison of experimental results to theory.

To realize different values of q_{eff} in the experiment, the mw frequency and thus the detuning δ_{mw} is changed. The value that is set in the script that programs the mw generator is q_{exp} and is expected to linearly influence q_{mw}, with a slope of approximately 1.

Over longer measurement periods (∼days), q_{eff} as a function of q_{exp} can shift. To track these shifts, SCC–spectroscopies can be performed([16, 17, 28]).

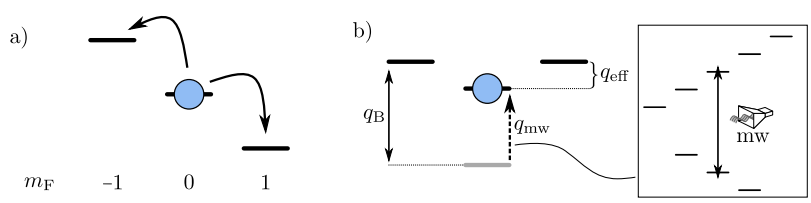

Figure 12: (a) Two particles in the $m_f = 0$ state scatter into an entangled pair with one particle in the $m_f = -1$ and on in the $m_f = +1$ state. (b) by off-resonant MW coupling of the $m_f = 0$ state to the F=2 hyperfine manifold, the quadratic zeeman shift can be experimentally controlled. Figure taken from [16]

5.2 Experimental investigation of spin dynamics

The objective of the presented experiments in this Section is to determine the values q_{eff} and $\tilde{c}_1$, where the latter locally represents the effective spin–spin interaction in our quasi–1d system. To do so, the experiments are locally (a region of $\Delta x \approx 4\mu\text{m}$ near the trap center) compared to a simulation of the EOM in the SMA ([18]) and ([19]), see Fig. 3, which is valid in the LDA (see Section 2.3). As discussed briefly in Section 2.3, the LDA is a valid approximation [15], if the state does not feature any spatial structure on the order of the spin healing length, which is roughly $\xi_s \approx 5\mu\text{m}$ [17]. This condition is mostly met in the observed dynamics and will be discussed after the following data analysis, at the end of this Section.

Different spatially homogeneous spin profiles were prepared, using the scheme presented in 4, without local imprint. The different initial conditions (IC) lie on the equator of the spin–nematic sphere, meaning they feature $F_z = 0$ and $Q_0 = 0$. They only differ in the spin length $F_\perp$, depending solely on the spinor phase 15, which is controlled by the holding time T_{hold} (see Fig. 9a). Their time evolution under different q_{exp} was tracked for ~ 0.5 to 0.7s seconds.

For each setting (combination of IC and q_{exp}), F_xF_y – and F_z –readout were performed subsequently. The evolution times were measured interleaved, meaning for each evolution time the settings were scanned through, before moving on to the next evolution time. The density profiles for different evolution times (averaged over all settings) and the total atom number in the selected region are shown in Fig. 13. The fluctuation in the total atom number is due to fluctuations in laser power during the measurement period ($\sim$ 1 day). Another reason may be sloshing of the condensate, as the fluctuation is on the order of the trap frequency in the x–direction. Note that the density profile is relatively rough, that is, it features ripples on the order of the spin healing length.

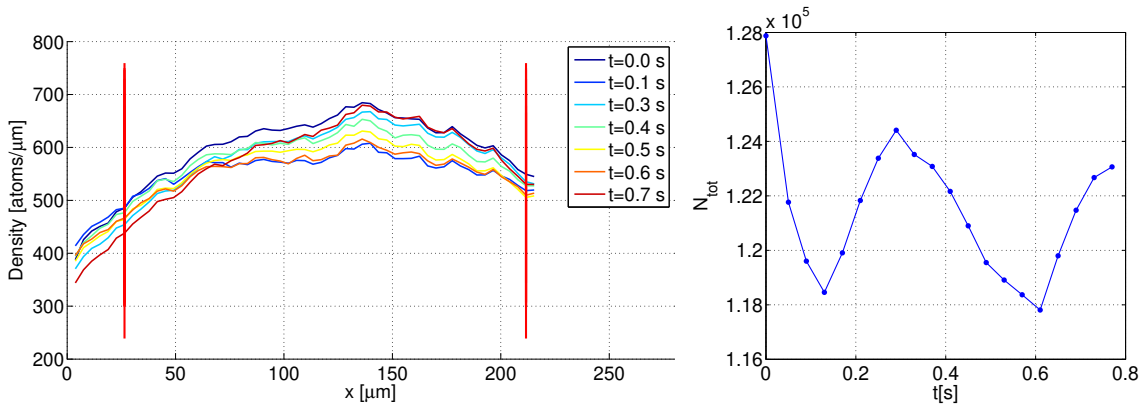

Figure 13: Left: Density profiles for different evolution times t, averaged over all settings. The red lines mark the region selected for further analysis. Right: total atom number as a function of evolution time t.

The data for three chosen settings is presented in Fig. 14. Each row shows the temporal evolution of the $F_\perp$, Q_0 and F_z profiles (left to right) for one setting, averaged over $\sim$12 realizations. Despite different IC's, each row shows a different q_{exp}. The data is binned with a relatively large bin size of 9 pixels ($\approx 4\mu\text{m}$) to minimize noise, especially since local cuts are presented, and no sharper features than that are observed.

Especially in the upper two panels, one can see in $F_\perp$ and Q_0 (left and middle), that no strong spatial structure is developing, except on the very edge of the condensate. The spin profile remains relatively flat and shows a global oscillation. One exception is a small dip in the spin length building up, especially for the latest evolution times (top left panel in Fig. 14). The position coincides with a small density peak (see13), which may be the reason for this deviation. The lower panel shows a stronger spatial dependence. This is because here, a spatial crossing of the separatrix is happening. As $\tilde{c}_1$ depends on the density, which is itself spatially dependent, the shape of the phase space in the LDA also varies spatially. Thus, the same spin state can lie on a trapped trajectory in the trap center, while experiencing a free–running time evolution on the edge. This could be seen even more clearly in the Larmor phase profile featuring two π–jumps at around 0.4s (as the spin direction in the free–running region flips) for the third setting in Fig. 14, which was observed but is not shown here, since the focus will be set on the spin dynamics in the trap center.

The right panel shows a build–up of a negative expectation value of F_z. This effect depends on q_{exp}, as the figure suggests, and is not fully understood. One possible explanation is that the atoms in the side modes experience a force due to a slight inhomogeneity in the offset B–field. It might also be related to demixing effects. Note that the side mode population is directly linked to Q_0, being maximal for $Q_0 = -1$ and minimal for $Q_0 = 1$, and that changes in F_z are especially strong in the upper panel, where also the side mode population is large. Another observed feature is that the negative F_z seems to be "seeded" at two positions ($\sim$ 80 and $\sim$ 160µm). This is even more prominent in the free–running trajectories presented in Appendix B.

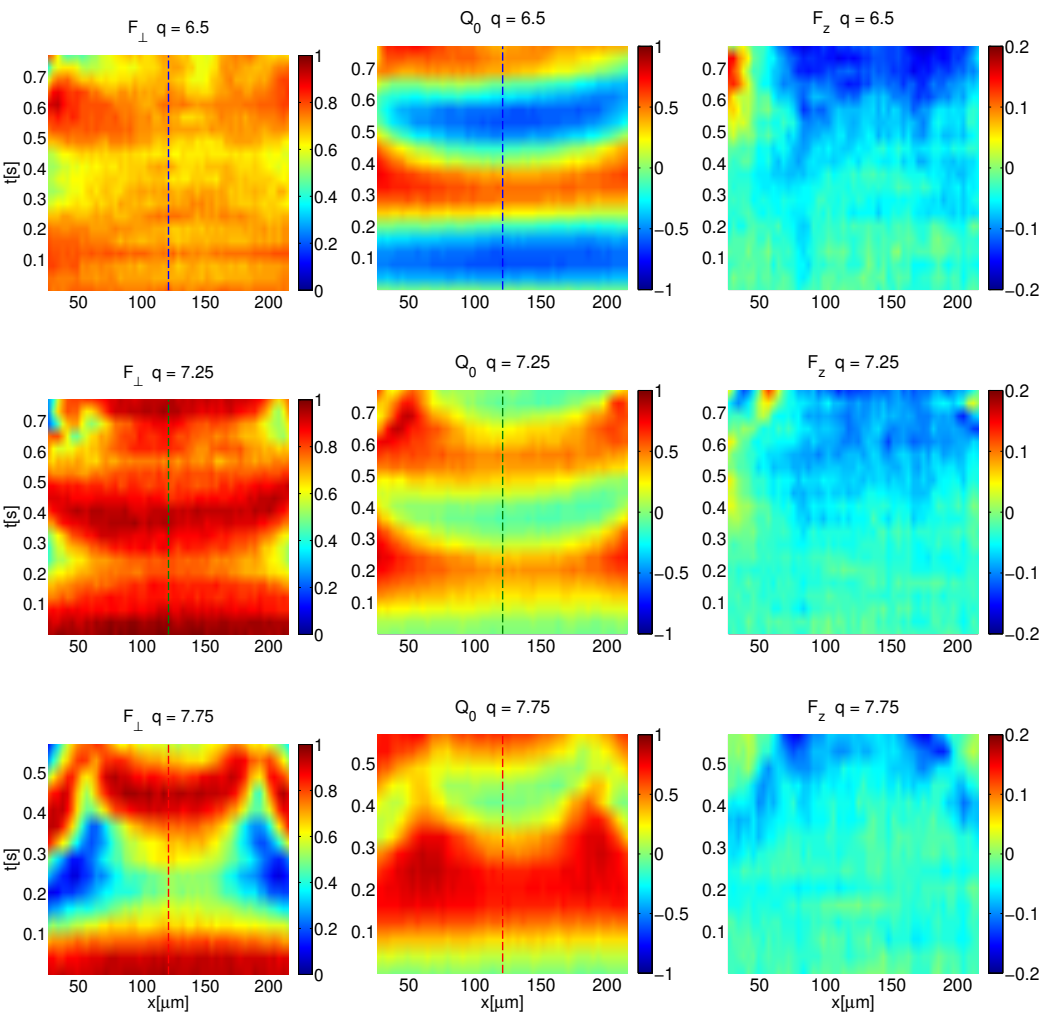

Figure 14: Each plot shows the time evolution of measured spin observables, with space on the x–axis and evolution time on the y–axis (increasing from bottom to top), averaged over ∼12 realizations. The three columns show $F_\perp$, Q_0 and F_z (left to right). Each row shows the time evolution of one specific initial condition (IC), for one specific q_{exp}, respectively (denoted by q in the captions). The different IC's are spatially flat and lie on the equator of the spin–nematic sphere, meaning they feature $F_z = 0$ and $Q_0 = 0$. They only differ in the spin length $F_\perp$. The dashed perpendicular lines in the $F_\perp$ and Q_0 plots indicate cuts at the position x_{cut}. They allow to read off the oscillation and the IC more easily (see Fig. 15).

Cuts in the center of the spatial $F_\perp$– and Q_0– profiles are presented in Fig. 15. They allow to read off the initial condition more easily than the full spatial profiles (Fig. 14). The rows refer to the same q_{exp} as in Fig. 14, respectively. The right panel shows the two oscillations in a $F_\perp$–Q_0–diagram, a projection of the spin–nematic sphere on the $F_\perp$–Q_0–plane. It visualizes how the system follows the known trajectories of the SMA (compare Fig. 2). A dampened sine curve is fitted to $Q_0(t)$ with the functional form

$$Q_0(t) = Ae^{-kt}\sin(2\pi(ft + d)) + Q_0^{\text{stable, fit}}, \tag{36}$$

where A is the amplitude, k is a damping factor, f is the oscillation frequency, d is a phase shift, and $Q_0^{\text{stable, fit}}$ is the offset of the oscillation. Although, the recorded

oscillations do not show a damping behavior on the timescale of this measurement, the damping factor is still kept to assure accurate estimation of the oscillation offset and frequency.

The three measurement settings presented were selected, because they each fulfill two advantageous criteria for a determination of q_{eff} and $\tilde{c}_1$: One being that they show trapped trajectories, so that the Q_0–offset ($Q_0^{\text{stable, fit}}$) directly gives the position of the stable point, and thus $q_{\text{eff}}/\tilde{c}_1$ via eq.24:

$$\left(\frac{q_{\text{eff}}}{|\tilde{c}_1|}\right)^{\text{meas}} = 2 \cdot Q_0^{\text{stable, fit}}, \quad \text{with the error} \quad \Delta\left(\frac{q_{\text{eff}}}{|\tilde{c}_1|}\right)^{\text{meas}} = 2\Delta Q_0^{\text{stable, fit}}. \tag{37}$$

Here, "meas" in the superscript indicates, that this is now a measured quantity. The error $\Delta Q_0^{\text{stable, fit}}$ is given by the 1σ confidence interval of the fit. The resulting values are presented in in the left panel of Fig. 16. Note, that Furthermore, the IC does not lie too close to the stable point, so that the oscillation amplitude is large enough to reliably obtain a frequency, but also not too close to the separatrix, where the oscillation deviates strongly from the sinusoidal shape, and the frequency is very sensitive to $q_{\text{eff}}/\tilde{c}_1$ and the IC. The sensitivity to the IC is seen in figure 3 (left panel), as the frequency freatures a sharp dip where the IC crosses the seperatrix. The sensitivity to $q_{\text{eff}}/\tilde{c}_1$ is due to the shift of this dip. The Spinor phase IC is calculated from the measured $F_\perp$ IC using eq. (15) as

$$\phi_S^{\text{IC}} = \cos^{-1}(F_\perp^{\text{IC}}), \quad \text{with the error} \quad \Delta\phi_S^{\text{IC}} = \frac{1}{\sqrt{1 - F_\perp^2}} \cdot \Delta(F_\perp^{\text{IC}}). \tag{38}$$

The error in $F_\perp$ is the standard deviation of the different realizations.

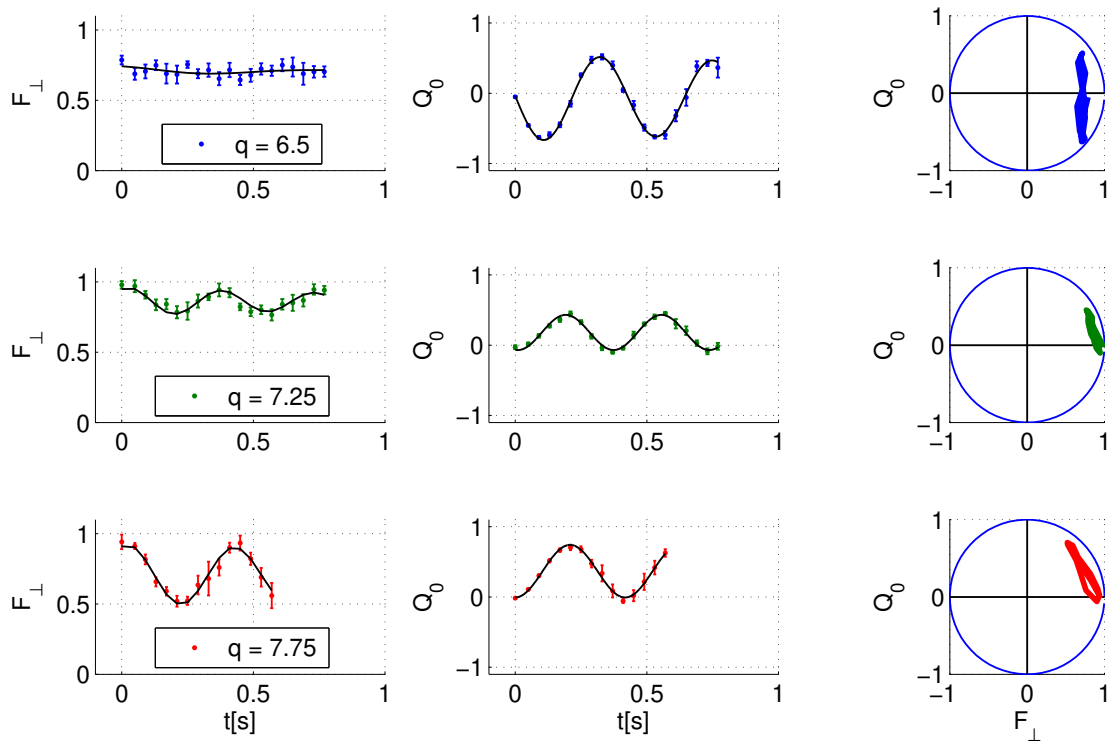

Figure 15: Left and middle: Cuts through the time evolution of the measured $F_\perp$ and Q_0 profiles at a single spatial position $x_{\text{cut}} \pm \Delta x$ with ($\Delta x \approx 4\mu$m given by the bin size). The black line in each plot represents a fit function. The functional shape of the fit function for $Q_0(t)$ is given by 36. The fit to $F_\perp$ is not used for further analysis. Each row presents one setting for q_{exp} (denoted by q in the labels). The right panel shows the trajectory on a projection of the spin–nematic sphere on the $F_\perp$–Q_0–plane. Error bars indicate the standard deviation of the single realizations.

For each of the three settings, a simulation of (18) and (19) is performed for the given ratio $(q_{\text{eff}}/\tilde{c}_1)^{\text{meas}}$ and ϕ_S^{IC}, to obtain the expected oscillation frequency f^{sim} in units of $\tilde{c}_1$. The error of f^{sim} is found by running the simulation for all nine possible combinations of $\left\{(q_{\text{eff}}/\tilde{c}_1)^{\text{meas}}, (q_{\text{eff}}/\tilde{c}_1)^{\text{meas}} \pm \Delta(q_{\text{eff}}/\tilde{c}_1)^{\text{meas}}\right\}$ and $\left\{\phi_S^{\text{IC}}, \phi_S^{\text{IC}} \pm \phi_S^{\text{IC}}\right\}$ and choosing the largest/lowest outcome as the upper/lower bound $f^{\text{sim, upper}}$ and $f^{\text{sim, lower}}$.

The estimated absolute value of $\tilde{c}_1$ in the experiment is then calculated in units of Hz as

$$|\tilde{c}_1^{\text{est}}|[\text{Hz}] = \frac{f[\text{Hz}]}{f^{\text{sim}}[\tilde{c}_1]}. \tag{39}$$

The asymmetrical error of f^{sim} is propagated to $\tilde{c}_1^{\text{est}}$ via

$$|\tilde{c}_1^{\text{est, upper}}|[\text{Hz}] = \frac{(f+\Delta f)[\text{Hz}]}{f^{\text{sim, lower}}[\tilde{c}_1]} \quad \text{and} \quad |\tilde{c}_1^{\text{est, lower}}|[\text{Hz}] = \frac{(f-\Delta f)[\text{Hz}]}{f^{\text{sim, upper}}[\tilde{c}_1]}. \tag{40}$$

Δf denotes the fit error of f, given by the 1σ confidence interval of the fit. It is negligible compared to the error of f^{sim}. The latter is significantly influenced by both the error $\Delta(\frac{q_{\text{eff}}}{\tilde{c}_1})^{\text{meas}}$, which originates from $\Delta Q_0^{\text{stable, fit}}$, and the error in the initial condition $\Delta\phi_S^{\text{IC}}$, which is especially large for elongated spins. The described method to determine $\tilde{c}_1^{\text{est}}$ is applied to the three measurements individually, and

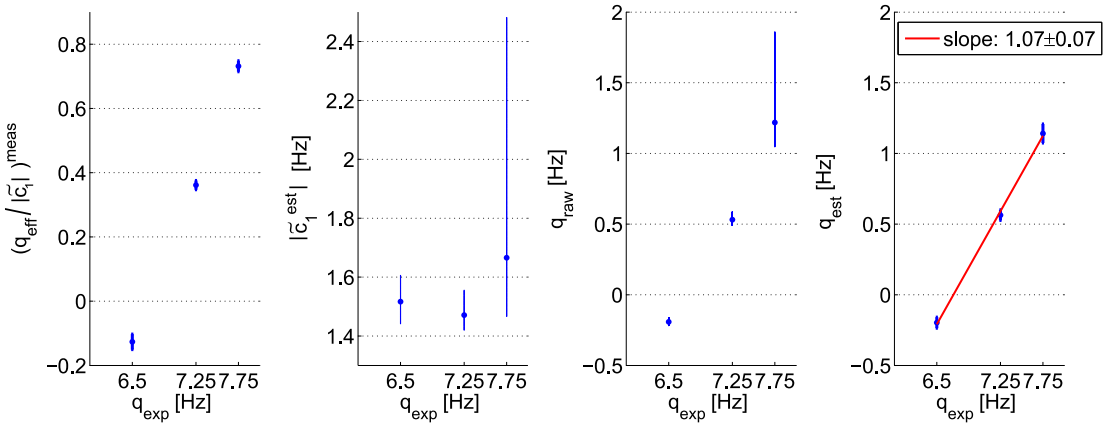

Figure 16: Left to right: The obtained values for (1) $(q_{\text{eff}}/|\tilde{c}_1|)^{\text{meas}}$, (2) $|\tilde{c}_1^{\text{est}}|$ (3) q_{raw} and (4) q_{est}. The red line in the rightmost plot is a linear fit, yielding a slope of ~ 1. $(q_{\text{eff}}/|\tilde{c}_1|)^{\text{meas}}$ is obtained from the offset of the Q_0 oscillation, $|\tilde{c}_1^{\text{est}}|$ is found by comparing the observed oscillation frequency f to a simulation of the EOM in the SMA (18,19), q_{raw} is the product of the data in the first two panels, and q_{est} is found by multiplying $(q_{\text{eff}}/|\tilde{c}_1|)^{\text{meas}}$ with the leftmost data point in the second panel.

the results are presented in the second left panel of Fig. 16. The outcomes are expected to be the same, and they agree within their error bounds to be roughly $|\tilde{c}_1^{\text{est}}| = (1.5 \pm 0.1)$Hz. The very large error for the third setting of q_{exp} is due to the proximity of to the separatrix and the relatively large error in the Spinor phase IC, partly leading to very small expected frequencies f^{sim} in the simulation.

The estimated value for q_{eff} in Hz is obtained by multiplying $(q_{\text{eff}}/\tilde{c}_1)^{\text{meas}}$ by the previously found $\tilde{c}_1^{\text{est}}$. Therefore, one can either use the individual results $\tilde{c}_1^{\text{est}}(q_{\text{exp}})$ of the different settings or use the value for $\tilde{c}_1^{\text{est}}$ that is expected to be the most reliable result. The first method yields q_{raw}, presented in the third panel of Fig. 16, featuring a large error for the third q_{exp}. The asymmetric error propagation is carried out analogously to eq. 40.

The second method uses $\tilde{c}_1^{\text{est}}$ from the first setting for two reasons: q_{eff} is very small, so the trajectory is almost solely dominated by a rotation around Q_0 given by $\tilde{c}_1$. It is reasonable to measure $\tilde{c}_1$ in this regime. Furthermore, the $F_\perp$ IC is not as elongated as in the other settings, so that eq. 15 and 38 are less likely to induce a systematic error due to some offset that should be taken into consideration (see, e.g., Fig. 9a). The results are presented in the right panel of Fig. 16, together with a linear fit, showing a slope of ~ 1. This satisfies the expectation that the experimentally set value q_{exp} describes a shift in units of Hz with an unknown offset.

During the period of the presented experiments, SCC–spectroscopies were performed, showing no significant shift of q_{eff}. The maximum of these spectroscopies was at $q_{\text{exp}} = 7$ to $q_{\text{exp}} = 7.5$ (with a step size of 0.5Hz). Using the results from the analysis performed in this Section, this roughly corresponds to $(q_{\text{eff}}/|\tilde{c}_1|)^{\text{meas}} \approx 0.4$. This is not a robust result but shall only serve as a broad orientation, as the spectroscopies were not evaluated in detail.

In addition to the three measurements presented, other combinations of q_{exp} and IC were also investigated: The elongated spin was found to be a globally stable state for $q_{\text{exp}} = 6.5$, as expected from the LDA. For the higher values of $q_{\text{exp}} = 7.25$ and $q_{\text{exp}} = 7.75$, the reduced spin lengths exhibits free-running behavior globally. These

measurements are shown in the Appendix B. The only instances where strong spatial structure emerged were those situated close to the separatrix, as the density profile became increasingly relevant for these IC's. It is anticipated that spatial structure will be formed in all settings within the easy–plane phase at a later point in time. This is because the accumulated phase difference for the different positions will eventually lead to the formation of structure. The greater the spatial dependence of any spin observables, the less likely it is that the dynamics can still be captured by the LDA, as the kinetic energy becomes increasingly relevant.

An indication that the simulation and the data are not compatible is the aforementioned build–up of a negative F_z expectation value in the data, while the EOM (18 and 19) strictly conserve $F_z = 0$ as given in the IC. Another indication that the LDA does not fully describe the time evolution in these experiments are artefacts like for example the small dip observed at late times in the spin length for $q_{\text{exp}} = 6.5$ (upper left panel in Fig. 14). The small peak in the density at this position does not explain this. Since the dip is quite sharp, it may be explained considering gradient corrections to the LDA [29]. The total density profiles vary with the evolution time due to the excitation of spatial modes in the trap, as well as fluctuations of the laser power, that affect the total atom number over the measurement period. Both effects distort the local density approximation, which does assume a constant density over time at a given position. The density fluctuations at the cut position evaluated in this experiment is on the order of 10%.

A feature that was observed but not fully understood is that the global Spinor phase IC for one specific T_{hold} appears to depend on q_{exp}. This may be explained by timing errors in the state preparation, which would be inconvenient and require further investigation.

6 Spin dynamics with local spinor phase rotation

The dynamics of spin profiles that feature a local rotation in the spinor phase is studied. The preparation of the local spinor phase rotations is discussed in section 4. First, the effect of a relatively weak imprint is compared to that of the same IC without a local imprint. The results of an experiment with a stronger imprint are then presented. Finally, a measurement is presented that features a vortex in space and time in the Larmor phase, and therefore might pose the possibility to experimentally generate an instanton.

6.1 Local spin oscillation

The cosine- shaped local imprint is realized with a series of 14 positions of the imprint with beam times between 1µs and 7µs, spaced by 0.14Mhz and an AOD power of 0.9V. For comparison, the same measurement was made without the local imprint. For each setting, F_xF_y – and F_z –readout were performed subsequently. The evolution times were measured interleaved. The data were binned with 3 pixels (as in all the following experiments), so that one bin corresponds to $\sim$ 1.3µm, which is roughly the optical resolution of the imaging. The results are shown in Fig. 17, where the rows show $F_\perp$, Q_0 and F_z for the measurements with imprint (top row) without imprint (middle) and the difference (bottom), respectively. For better visibility, the latter is presented in black and white color code. In Q_0, one can see a local oscillation. The $F_\perp$–profiles feature a local dip exhibiting an oscillation as well; however, this oscillation is at a lower frequency than the one observed in Q_0. The measurements without the imprint show the behavior discussed in Section 5.2. Subtracting the reference without imprint allows to investigate the effect of the imprint, especially in Q_0, where the "background"–oscillation is larger. The result in the lower middle panel shows the symmetric outward radiation of a dip, with a velocity of roughly 200µm s^{-1}, which is a clear deviation from the LDA. It originates at the first minimum of the Q_0 oscillation at the imprint center. Another wave seems to be emitted at the second minimum ($\sim$ 0.4s), but this is not clearly visible. For comparison, the spin speed of sound for a local perturbation in the Larmor phase was measured to be 110µm s^{-1} in [30]. The $F_\perp$ profiles do not feature this outward–radiation. The F_z profiles show that the local imprint delays the build–up of negative F_z in the center. Next to the imprint position, F_z is more negative than without imprint.

As in the previous section, cuts through the $F_\perp$ and Q_0 profiles are presented, with a dampened sine fit, as well as a visualization of the trajectories in the $F_\perp$–Q_0 plane (see Fig. 18). The trajectories with (green) and without imprint (blue) show a similar offset ($\sim$ 0.08) in Q_0, which is expected in the LDA (as it does for trapped oscillations not depend on the IC). With the imprint, the frequency of the Q_0 oscillation ($f_{Q_0}^{\text{impr}} = (3.00 \pm 0.06)$Hz) is smaller than without the imprint ($f_{Q_0}^{\text{no impr}} = (3.16 \pm 0.07)$Hz), which is also expected from an LDA, as the imprint locally brings the profile closer to the separatrix. The very low offset in Q_0 indicates q_{eff} close to zero, so that the separatrix would almost touch the south pole of th spin–nematic sphere.

Without imrpint, the oscillation frequencies in $F_\perp$ and Q_0 agree within their error bars (given as the 1–σ confidence interval of the fit function). However, with

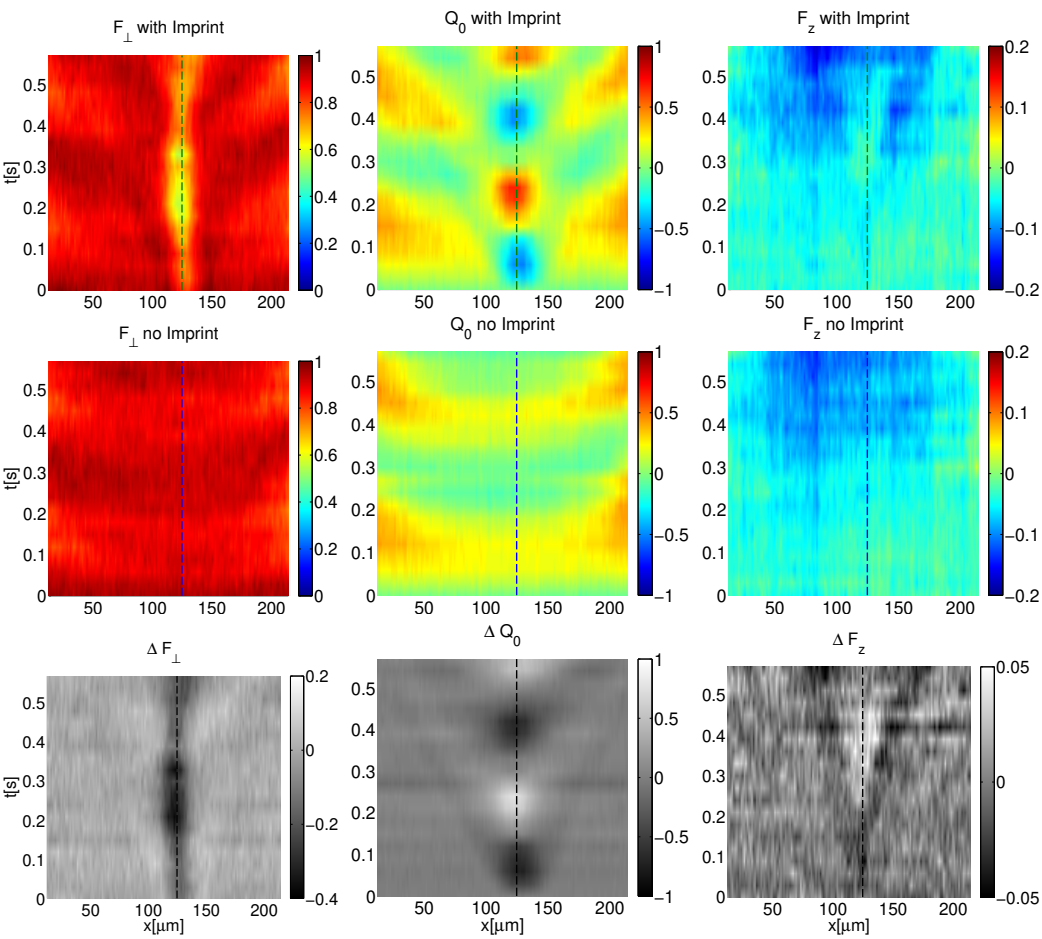

Figure 17: Each plot shows the time evolution of measured spin observable with space on the x–axis and time on the y–axis, averaged over ~ 12 realizations. The three columns show $F_\perp$, Q_0 and F_z (left to right). Top: the IC features a local spinor phase rotation. Middle: no local modulation. Bottom: difference between the two upper rows. The dashed perpendicular lines in the $F_\perp$ and Q_0 plots indicate cuts at one spatial position (see Fig. 18).

the imprint, the frequencies in $F_\perp$ ($f^{\text{impr}}_{F_\perp} = (2.1 \pm 0.2)$Hz) and Q_0 ($f^{\text{impr}}_{Q_0} = (3.00 \pm 0.06)$Hz) do not agree. This is not fully understood. One possible explanation could be changes in the total density. The total atom number as a function of evolution time looks very similar to Fig. 13 (right), which shows fluctuations roughly on the 2Hz frequency that is also seen in $F_\perp$. The density oscillation changes $\tilde{c}_1$ and is superimposed with the spin mixing dynamics. In $F_\perp$ this superposition is expected to be seen more pronounced, since the oscillation amplitude in the chosen setting for small q_{eff} is much smaller than in Q_0. It could also be due to effects of the kinetic energy, showing a deviation from the LDA. To support this, the density effect would have to be ruled out.

Due to the stray light problem for IC's with imprint, the IC in the spinor phase can not be measured reliably, and the observed trajectory is thus not quantitatively compared to a simulation of the LDA. Note also that the error bars for the oscillation with imprint are much larger, mostly due to the noisy preparation of the IC, but also due to the stronger proximity to the separatrix. The result of this analysis is that the time evolution of a profile with a relatively small imprint can still

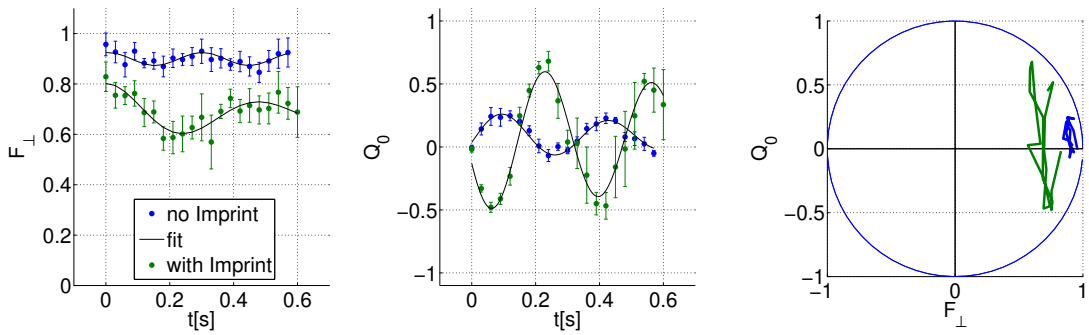

Figure 18: Left and middle: Cuts through the time evolution of the measured $F_\perp$ and Q_0 profiles at the center of the imprint. The blue data points refer to the reference measurement without local imprint, the green points refer to the measurement with the imprint. The black line in each plot represents a fit function, which is for $Q_0(t)$ given by eq. 36 as in the previous section, for $F_\perp$ its the same fit function, by just replacing Q_0 with $F_\perp$ in the variables. The right panel shows the trajectory on a projection of the spin–nematic sphere on the $F_\perp$–Q_0–plane. Error bars indicate the standard deviation of the single realizations.

be qualitatively understood by the LDA, but significant deviations are seen in all measured observables.

6.2 Leaving the trapped region locally

As in the previous section, a cosine–shaped imprint is realized. In comparison to the previously presented one, all settings vary to some extent in this measurement. The number of imprints is reduced to 10 (was 14), which allows a shorter holding time T_{hold} (is reduced from 500.5µsto270.021µs). The idea behind this is that shorter holding times might reduce noise in the IC. The shortest pulses used previously were below 2µs and therefore too short for an imprint anyway. The horizontal spacing was somewhat enhanced (0.1MHz to 0.15MHz), to allow a larger imprint using fewer pulses. Also, q_{eff} might be somewhat different. The oscillation in the background of Q_0 allows a very crude estimate of $\sim 0.4\tilde{c}_1$ at the edge (maxima and minima in Q_0 are read from the color scale to be approximately -0.3 and 0.7, so the offset is around 0.2), based on eq. 37).

The main difference in the IC is that the background spin length is shorter (due to different T_{hold}) and the imprint is deeper. The former causes a larger background oscillation, the latter causes the system to locally (at the imprint position) leave the trapped region on the spin–nematic sphere. The spatially resolved time evolution of $F_\perp$, Q_0, ϕ_L and F_z is presented in Fig. 19. $|\langle F_\perp \rangle|$ (upper left) is the absolute value of the mean complex valued $F_\perp = F_x + iF_y$ over (~ 12) realizations. Since a global Larmor phase is randomly given in the single realizations due to fluctuations of the offset B field, the single realizations are rotated onto each other on the left edge of the region of interest, and then averaged. Otherwise, they would average to zero. The Larmor phase (lower left) is the Larmor phase of the mean $\langle F_\perp \rangle$, as one can see on the left edge it is set to zero. Therefore, it is the Larmor phase in the rotating frame of the Larmor frequency at the left edge. Q_0 and F_z are extracted from the F_z readout that is performed interleaved, and also averaged over ~ 12 realizations.

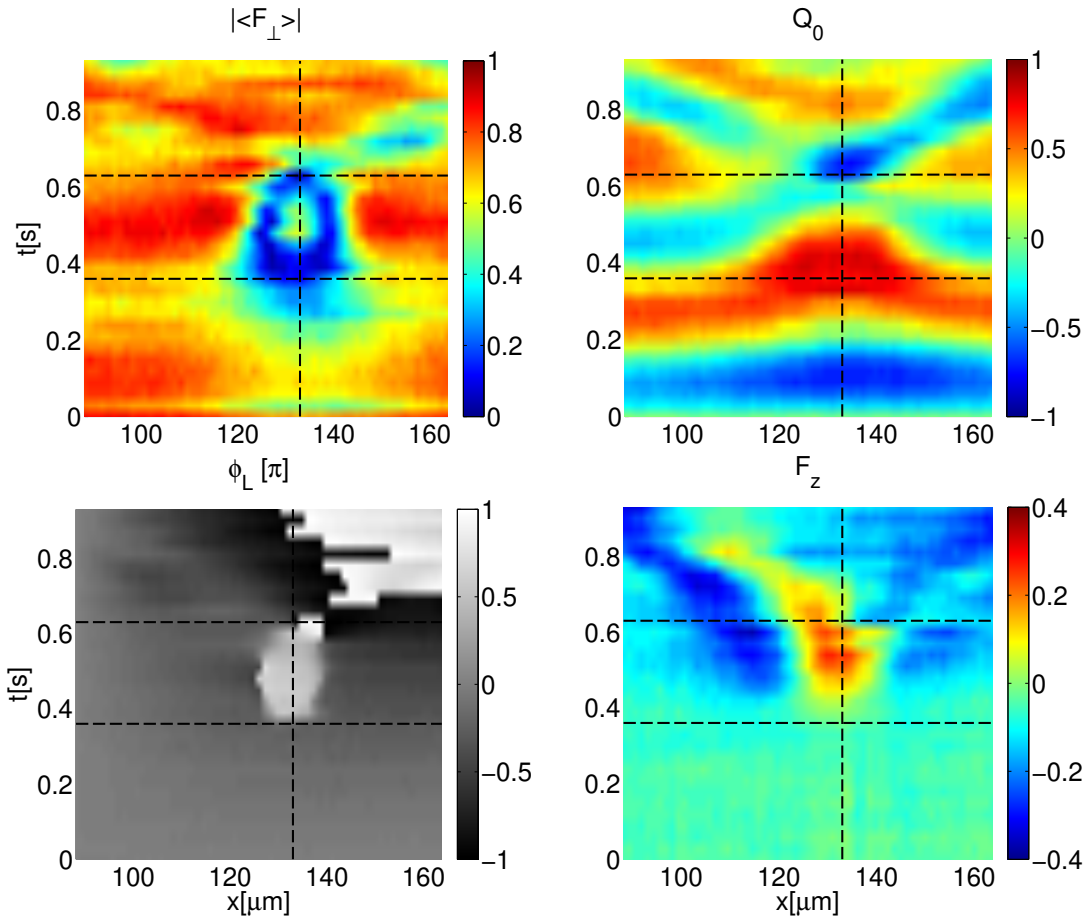

Figure 19: Each panel shows the time evolution of measured spin observable with space on the x–axis and time on the y–axis, averaged over ∼12 realizations. $|\langle F_\perp \rangle|$ and ϕ_L (upper and lower left) are absolute value and angle of the averaged complex valued transveras spin $\langle F_\perp \rangle = \langle |F_\perp| e^{i\phi_L} \rangle$. The initial condition in $|\langle F_\perp \rangle|$ is not reliable, as it is strongly influenced by stray light. Upper and lower right show Q_0 and F_z. The dashed black lines are a guide for the eye for comparing the four plots.

Following the perpendicular dashed line, one can see that $|F_\perp|$ goes to zero at around 0.4s and increases again afterwards. The Larmor phase shows that this increase of spin length is into the opposite direction, as there is a (π–) jump. On the left and right of the dashed line, the spin remains zero for some time, until the two dips converge and collide at around 0.6s. After that, the $F_\perp$ profile, as well as the Larmor phase, are more homogeneous again. Note that the "jump" from $-\pi$ to π (black to white) at very late times in the Larmor phase is not a real phase jump, as the values are continuously connected, but strongly distinguished by the color scale. Overall, one can see that the locally free–running trajectory leads to the build–up of a small domain with opposite spin direction encapsulated by the two dips (domain walls), that eventually collide and close this domain again. This domain can be nicely seen in the Larmor phase (bright region in the center). The LDA helps to understand the initial dynamics, but as the time evolution goes on, sharp features emerge, and kinetic energy strongly affects the dynamic behavior.

F_z shows a strong response to the imprint. In contrast to the previously observed broad build–up of a negative expectation value, here we locally see a positive F_z

building up after around 0.4s. Note that at ∼0.4s, around the imprint position the side mode population is very low (see large Q_0) so that F_z naturally can not show large expectation values. Further away from the imprint position, the background tends towards negative F_z. Especially on the left this is very pronounced, with values reaching $F_z \approx -0.3$ at around 0.6s. Interestingly, the broad peak at the imprint position seems to split up into a pair of a peak (left) and a dip (right) propagating outwards. This splitting coincides with the collision of the domain walls in $F_\perp$.

Q_0 shows the most oscillatory behaviour of measured observables. On the edge, one can see a rather undisturbed background oscillation. In the center, one sees an oscillation as well. The frequency is lower than on the edge, and goes towards quite large Q_0. Both indicates that the state does locally move on a free–running trajectory, which is still close to the separatrix an thus features low frequency and large amplitude. Neither the strong response in F_z nor the local change in spin–orientation ($F_\perp$ and ϕ_L) are visible in Q_0. The latter is because a trapped and free–running trajectory can look very similar in Q_0. At around 0.6s, the oscillation on the edge and at the center are just out of phase. Simultaneously, the collision of the two kinks in $F_\perp$ ocuurs. It looks like at this point, the spin–vector does locally change the transversal spin orientation by moving across the south pole of the spin–nematic sphere. Note, however, that since $F_z \neq 0$, the state can not be represented on the surface of the spin–nematic sphere, and this is just a qualitative discussion of the measurement results. This experiment shows how, if the system locally sits on a free–running trajectory, clear deviations from the LDA are visible. It could be very interesting to look at the mean–field energy functional to analyse how energy is moving in space and transferred between different degrees of freedom in time.

6.3 Towards creating a vortex in the Larmor phase

This measurement is meant to show that the local spinor phase imprint together with a B–field gradient might offer a possibility to deterministically generate a vortex in the Larmor phase. The conceptual idea is as follows (starting with a flat Larmor phase profile):

- Left edge: Larmor and spinor phase stay at rest (in the rotating frame of the Larmor phase).
- Right edge: The B–field gradient induces a 2π–winding of the Larmor phase relatively to the left edge. The spinor phase does not change.
- Center: The B–field gradient leads to a winding of 1π in the Larmor phase. Additionally, the spinor phase imprint leads to an evolution of 1π in the spinor phase, as the imprint locally puts the system on a free–running trajectory on the spin–nematic sphere in the LDA.

⇒ The left and the right edge differ by 2π in the Larmor phase (same spin orientation), while the rotation of π in both the Larmor and spinor phase at the center also results in the same spin orientation as in the beginning.

While the time evolution of the Larmor phase is determined by the B–field, the evolution of the spinor phase at the imprint position is susceptible to the density (via $\tilde{c}_1$), q_{eff}, the imprint depth (ϕ_S^{IC}) and most probably the imprint width and shape.

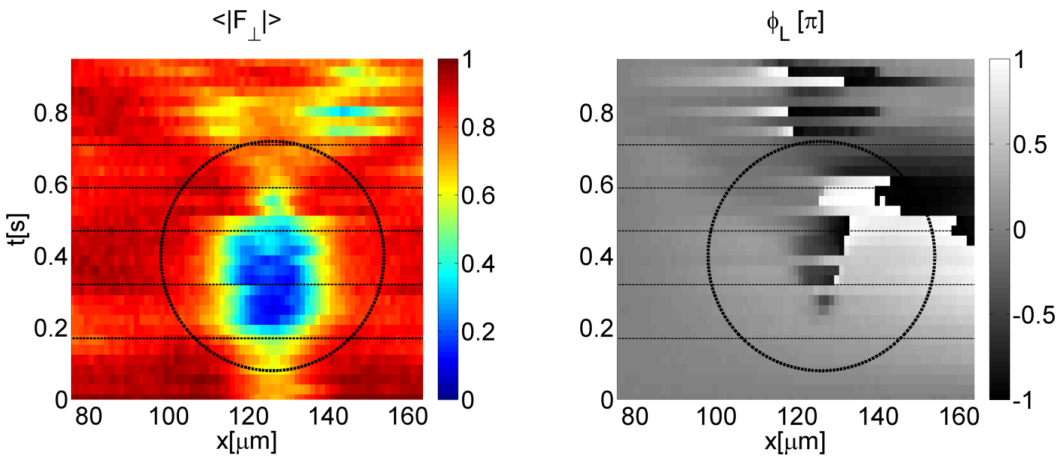

Figure 20: Left: Average $|F_\perp|$ profiles over ~ 12 realizations for evolution times up to 1s. The single realizations are averaged after taking the absolute value individually. Right: Time evolution of the Larmor phase. It is obtained by rotating the single realizations in $F_\perp$ onto another before averaging and taking the angle of the resulting mean. The black circle indicates a winding of 2π along its path. The horizontal cuts are presented in Fig. 21 in more detail.

The two timescales have to be matched, posing an experimental challenge, as both are not highly controllable. The dynamics between the three orientation points (left edge, center, and right edge) is to be studied, as well as the time evolution after the vortex is accomplished.

The presented measurement features a cosine-shaped imprint, using 14 imprint positions spaced by 0.14MHz, with beam times τ_B between 1µs and 7µs. The IC is comparable to the previous section although the background spin is more elongated (~ 1), and the imprint is somewhat less deep. As before, stray light prevents an exact knowledge of the IC. Also, q_{eff} might be somewhat different, the relatively small background oscillation at large $F_\perp$ indicates q_{eff} close to zero. Q_0 and F_z were not measured in this experiment, as it was chronologically the first one to be performed, and the F_z–readout was added to the experiments only later. The main difference to the experiment in the previous section is a small B–field gradient over the condensate. It is on the order of 0.01‰($\sim 10^{-5}$G) over 100µm, and thus does not significantly affect the second–order Zeeman shift, but it leads to the continuous build–up of a Larmor phase gradient. This phase gradient is associated with a different orientation of the transverse spin $F_\perp$ (see eq. 14), and also with a velocity of the side modes in opposite directions. Fig. 20 shows the time evolution of $\langle|F_\perp|\rangle$ and ϕ_L. The former shows a qualitatively comparable behavior to the $|\langle F_\perp\rangle|$ profile in the last section (see Fig. 19). Locally, the spin length goes to zero at around 0.25s. In this experiment, it does not return as clearly and the two dips on the left and right are not as prominent, as observed in Section 6.2. This is followed by a sharp dip at the imprint position at around 0.6s. After that, the profile is relatively flat again, while it seems like two broad dips radiate outward.

Note that $\langle|F_\perp|\rangle$ is determined differently than in the previous section. Rather than averaging the complex –valued data and then taking the absolute, here $\langle|F_\perp|\rangle$ is calculated by first taking the absolute of the single realizations and then averaging the absolute values. The reason for this is that the former method would lead to $|\langle F_\perp(x)\rangle| = 0$ for a large region in the center due to differing spin directions in

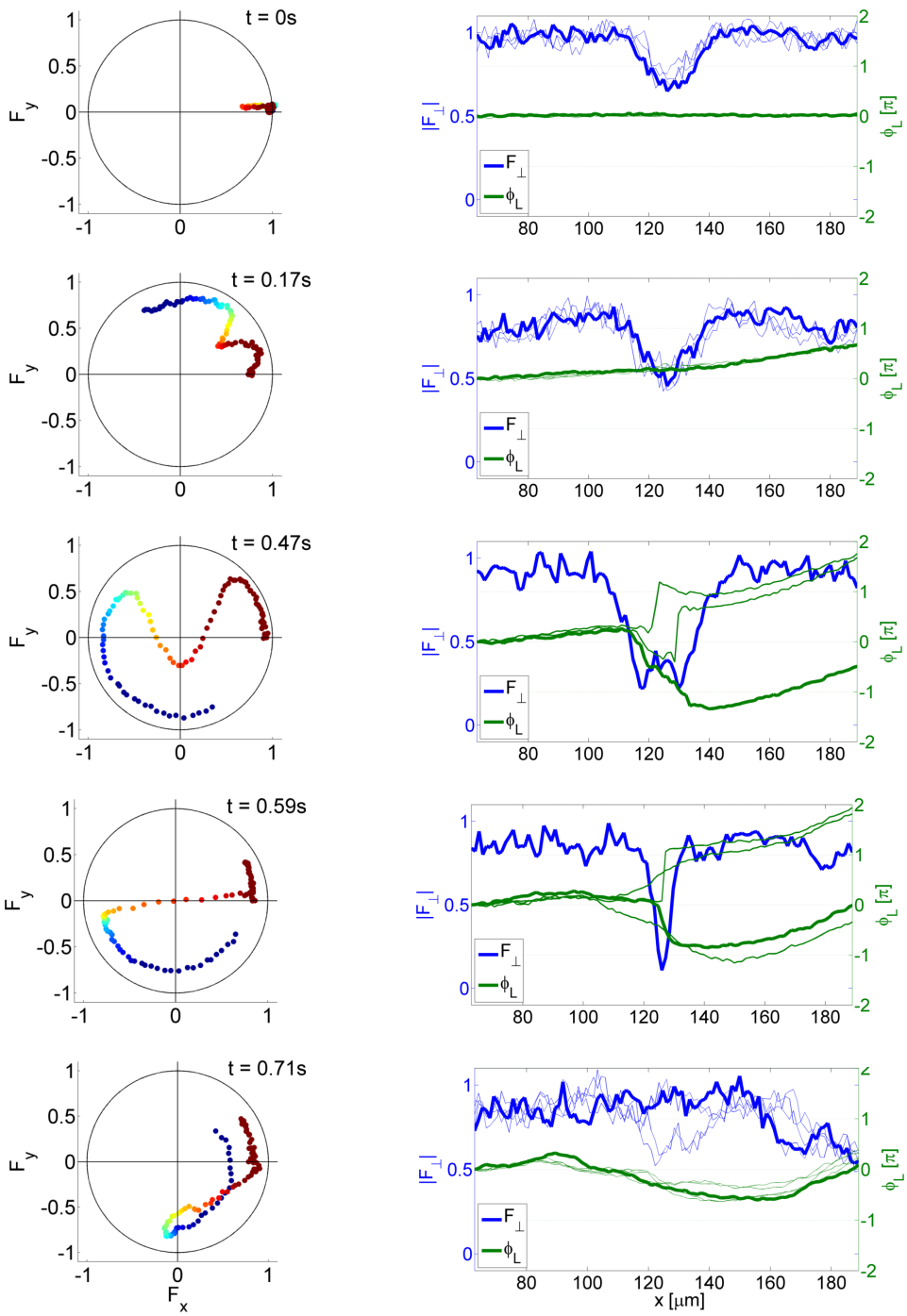

Figure 21: Left: Averaged $F_\perp$ profiles in spin space. The color code indicates the spatial extension (see right) with dark red being the left and deep blue being the right edge. Right: Spin length $|F_\perp|$ (blue) and Larmor phase ϕ_L (green) of chosen single realizations. Bold blue and green curves belong to the same realization, and are chosen, as they mostly resemble the mean shown left. Light curves show other realizations at the same time. The top panel left and right shows the IC, where the spin length is somewhat overestimated due to stray light.

the single realizations for most of the times after ~ 0.7s (a comparison is shown in Appendix C). After the sharp dip in the spin length at 0.6s, the single realizations become very different, and thus hard to average. For the Larmor phase, the method

from last section of first rotating the single realizations onto another, and then averaging was adopted, since otherwise it is impossible to obtain a reasonable signal. As large jumps in the Larmor phase (together with dips in $|F_\perp|$) do in single realizations often go in different directions, even though the complex $F_\perp$ almost looks the same, it cannot be taken from single realizations and then averaged, as $|F_\perp|$. The Larmor phase in the right panel of Fig. 20 shows a 2π–winding around the black circle.

For a better visual understanding of this observed vortex in the Larmor phase, another representation of the same data set is given in Fig. 21. The left panel shows the averaged complex valued $F_\perp$ for different selected times (indicated by horizontal lines in Fig. 20), the spatial dimension is represented by the different colors. The different realizations are rotated onto another, so that the left edge corresponds to $\phi_L = 0$. One can see the build–up of the Larmor phase gradient in this representation, as the blue end shows a rotation around the center. The imprint allows the state to locally leave the trapped region ($t = 0.47$), as the profile locally crosses the center of the plane. The combination of both effects allows to reach a state at $t = 0.71$s, where the $F_\perp$ has fulfilled a full rotation, however, it does not enclose the center.

The right panel of Fig. 21 depicts the $|F_\perp|$ and ϕ_L profiles of some chosen single realizations. One realization that mostly resembles the mean shown on the left is always bold. The Larmor phase has been unwrapped along the spatial dimension for this representation, that is, for any jumps larger than $\pm\pi$, multiples of $\pm 2\pi$ are added, so that the phase shows a smooth behavior, and the definition range is no longer limited to $[-\pi, \pi]$. The very upper plot shows the IC, but can only be interpreted qualitatively, as stray light significantly affects the $F_\perp$ readout. The second time step shows the continuous build–up of the Larmor phase gradient. At the time $t = 0.47$s, where the imprint has led to a crossing of the center of the plane, the Larmor phase shows two jumps that are very different for different single realizations. Physically there is not a large difference, since each realization might cross the center sightly different, therefore leading to a very different behavior of the Larmor phase. Note that the different values of the Larmor phase on the right of these jumps only differ in $\pm 2\pi$. At $t = 0.59$ s, where the sharp dip in $|F_\perp|$ appears, the Larmor phase has a $\pm\pi$–jump. The sign of the jump does not have a physical meaning here either, since it just depends on the exact position of how the system crosses the center and is therefore different in the single realizations. Just after the jump, the difference in $+\pi$ and $-\pi$ becomes relevant, since both $|F_\perp|$ and ϕ_L tend to flatten again. Here, interestingly, it is observed that the $-\pi$–jump was preferred. This seems somewhat intuitive, as due to the gradient that is continuously building up during the time evolution, the system can much easier "reconnect" the dip in this direction. The dip at $t = 0.59$second is very sharp (~ 10µm), goes to $|F_\perp| = 0$, and connects two points with opposite transvrsal spin direction. As the dip disperses, the spin at the center has to take a certain orientation again. As the domains to the left and right of the dip rotate with respect to each other, only one choice of orientation at the center actually decreases the spatial gradient in $F_\perp$. At 0.71s, one can clearly see, that while the Larmor phase at the right edge of the condensate has performed one full rotation, while its value at that position is not 2π, but 0. This is not an artifact as in the jumps observed at earlier times ($t = 0.47$s and $t = 0.59$s), as $|F_\perp|$ is not close to zero here, and the Larmor phase does not show any jumps. This effect is seen as a vortex in the Larmor phase in space and time.

Recalling the definition of the winding number 25, it is clear that in the experiment this exact definition cannot hold, as there are no periodic boundary conditions. However, for a certain spatial region, a winding number can be defined as

$$Q_w^{\text{exp}} = \frac{1}{2\pi} \int_{x_1}^{x_2} dx \frac{\partial \phi_L}{\partial x} = \phi_L^{\text{unwrapped}}(x_2) - \phi_L^{\text{unwrapped}}(x_1), \tag{41}$$

with $\phi_L(x_1) = 0$ it is given as $Q_w^{\text{exp}} = \phi_L^{\text{unwrapped}}(x_2)$ and can take continuous values. It is for the same region as in Fig. 21 ($x_1 \approx 70\mu\text{m}$, $x_2 \approx 190\mu\text{m}$) depicted in Fig. 22. The Figure shows the winding number of the single realizations as well as a majority vote. One can see that initially it is rising due to the B field gradient. As the broad dip in $|F_\perp|$ reaches zero, the winding number starts to jump up and down, differently in each single realization. As long as the $|F_\perp|$ profiles feature a dip close to zero, the winding number is not a particularly meaningful value, as even some noise might induce a difference of ± 1. It is however meaningful as soon as $F_\perp(x)$ does not get close to zero. At $t \approx 0.7$s, the winding number for most of the realizations is 0, concomitant with a spin length above 0.5 for most of the realizations, meaning a jump has occurred. Without the imprint, the system would have collected a winding number of 1 at this point. At $t \geq 0.8$s, this trend of preferring the lower winding number is not visible anymore and the majority vote jumps up and down again, as also the single realizations don't show a trend. The initially very linear increase of the winding number (modulo 1), also shows some deviation for later times. This can be caused by both, a change in the B field gradient, and the stronger influence of the imprint at the edge of the region of interest for later times.

To conclude, the winding number does not show one clean jump, which would have been the most clear signal indicating an instanton event. It shows several jumps and does not have a clear trend after $t \approx 0.8$s.

Even though in this experiment, looking at the winding number does not lead to a conclusive result, it offers a convenient way of analyzing the data, as it does not rely on averaging and furthermore avoids looking at all the single realizations.

Note, this measurement was not reproduced. This is mostly due to difficulties reproducing the exact B-field gradient. Furthermore, after the sharp dip at $t = 0.59$s, the single realizations differ strongly, and it becomes increasingly difficult at later times to average the data in a meaningful way. As one can see in Fig. 20, shortly after $t = 0.71$s, the mean Larmor phase behaves very differently for each time step, and it seems somewhat arbitrary to draw the circle in a way that it features a winding of 2π along its path. This is partly why Fig. 21 is presented, with the left panel showing the average over all realizations, to stress that the vortex was actually observed, undermined by the single realizations in the right panel. The reason why after $t = 0.59$s the single realizations differ strongly is probably because the exact configuration at this point is very crucial for the further time evolution of the state. The role of the B–field gradient is also not fully understood yet. Since it is generated with a coil that is not actively power–stabilized, slight changes in this gradient might also, especially after $t = 0.59$s, lead to a very different time evolution of the state. Shot–to–shot noise in the IC is also a possible explanation for this problem. As the complex data of the single realizations have to be rotated before averaging, this poses another possibility to "manipulate" the data, since the outcome after averaging depends on the position, where the data are rotated onto another.

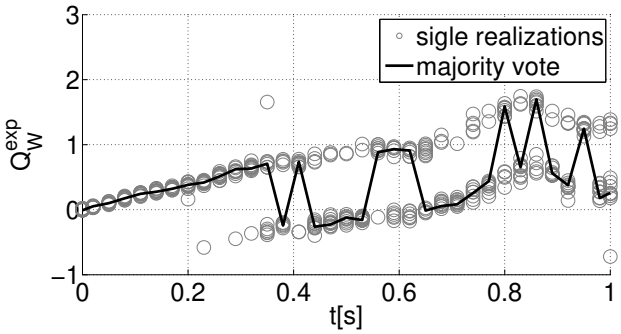

Figure 22: Winding number as a function of evolution time. It is defined as the unwrapped Larmor phase at the right edge of the region of interest, while the Larmor phase at the left edge is set to zero. The grey circles represent the single realizations, and the black solid line shows the majority of the single realizations. Initially only the build–up of a Larmor phase gradient can be seen, as the winding number continuously increases. As $F_\perp$ crosses the center, the Larmor phase jumps in most realizations. Around 0.7s, most realizations feature the lower winding number. Later the signal is very noisy.

As F_z and Q_0 were not measured in this experiment, it also remains open what is happening in these observables. The results of Section 6.2 might give an indication, since $|F_\perp|$ shows a comparable behavior there. An open question is also the comparability to the vortices observed in [13], since there the vortices are triggered by rogue–wave like events in the phase velocities in the single components. There have also been unpublished results with comparable IC's as in this experiment by the theory side, showing comparable results.

7 Conclusion and outlook

In the course of this thesis, different experiments were performed with a quasi-one-dimensional spinor BEC of ^{87}Rb atoms.

A scheme for the preparation of states that feature a local rotation of the spinor phase has been developed and tested in the experiments. The dependence of the spin length on the holding time T_{hold} shows that the relative phases of the mw pulses change with their temporal separation, giving rise to a very fast oscillation. This oscillation of roughly 15MHz comes from the frequency that is added to the signal of the mw generator in the I/Q–mixer.

An analysis of the imprint shape employing three subsequent beams in vertical direction with the same horizonatal position shows good agreement with a Gaussian shape in the modulated spinor phase. The imprint width is $\sigma_B = (5.7 \pm 0.7)$µm, and the horizontal jitter is $\sigma_{\text{pos}} = 0.7$µm. Fluctuations in the depth of the imprint are found to be on the order of 0.1π. The density profiles show over densities at the beam position for all beam powers, reaching up to $\sim 10\%$ for the strongest imprint (powAOD = 1.5V, $\tau_B = 12$µs). For the large over densities a splitting of the peak in the density is observed. Both density effects (over density and splitting) lead to a damping of the imprint depth as a function of beam time τ_B. Analyzing the latter, it is concluded that a time of roughly 2.5µs is needed for the sound wave in the AOD to build up. The most linear behavior of imprint depth vs. beam time was seen for AOD powers of 1V to 1.3V. The local imprint was also found to cause stray light on the camera in the initial condition, which can be minimized for horizontal beam positions using values of $f_{\text{AOD, h}} \leq 97.6$MHz. The density effects can be minimized by optimizing the wavelength of the local imprint laser. An improvement to the analysis could be to perform the experiments at a different background spin length, to be more sensitive to small imprints, and to distinguish actual fluctuations in the imprint depth from fluctuations in (insensitivities to) the background spinor phase.

As the F_z–redout is not affected by stray light, it is concluded from other experiments that the imprint does not have a significant effect on F_z and Q_0. It also does not affect the Larmor phase.

Spatially flat spin profiles were prepared and their time evolution under different second–order Zeeman shifts q_{eff} was investigated. The profiles qualitatively show to locally follow the trajectories predicted by the single–mode approximation, motivating the applicability of the local density approximation. Both trapped and free–running trajectories were observed, as well as configurations, where the system divides into trapped and free–running regions, depending on the local density. The offset of trapped oscillations of $Q_0(t)$ in the trap center enabled us to determine the relative position in the easy–plane. A comparison of the observed frequency with a simulation of the spin equations of motion in the single–mode approximation reveals the second–order Zeeman shift q_{eff}, and the local value for an effective spin-spin interaction strength $(\tilde{c}_1)^{\text{est}}$. The latter is the product of an effective one-dimensional local density n^{1d} and the effective one–dimensional spin coupling constant c_1^{1d}. Although it is not clear what n^{1d} and c_1^{1d} exactly are, the most relevant parameter in the experiment is in our case the combined value $\tilde{c}_1$. For the estimated spin interaction $(\tilde{c}_1)^{\text{est}}$, consistent results of $|\tilde{c}_1^{\text{est}}| = (1.5 \pm 0.1)$Hz are obtained. The obtained values for the second–order Zeeman shift q_{est} confirm the expected linear dependency on the value that is set in the control of the experiment, with a

slope of $(\Delta q_{\text{est}})/(\Delta q_{\text{exp}}) = 1.07 \pm 0.07$. Note that even though these results are self–consistent, there may be systematic errors, as the method is built on the LDA.

This analysis could be further improved by not only comparing the results in Q_0 with the simulation, but fitting the exact functional shape to the observed trajectories in $F_\perp$ and Q_0. The method presented in this thesis uses sinusoidal fits that do only in some configurations resemble the trajectories that are in general described by elliptical sine functions [14]. The state preparation used in these experiments showed an unexplained dependence of the spinor phase initial condition on the programmed value for the second–order Zeeman shift q_{exp}.

The analysis of spin dynamics featuring the local spinor phase rotation in the initial condition focused on two scenarios. The first one being a state that was globally and locally on a trapped trajectory, with the same spin orientation (slight local imprint). This leads to an evolution that still resembles the local density approximation but showed some differences, as wave packets in Q_0 seem to radiate outward from the locally different oscillation. A slight effect of the imprint on the evolution of the vertical spin F_z is observed. An anomalous low frequency oscillation in $F_\perp$ at the imprint position remains unexplained. Here, numerical simulations could provide a good sanity check, even on a mean–field level.

A complete deviation from the local density approximation is observed for an initial condition, that is globally trapped but locally sits on a free–running trajectory. Here, a spin domain of opposite spin direction is formed temporarily. This effect is accompanied by strong excitations in the vertical spin.

Finally, a measurement is presented that aims towards the deterministic creation of a vortex in the Larmor phase. The vortex can be observed in the Larmor phase when choosing the right path through its spatio–temporal evolution. Obtaining a decent signal for the Larmor phase is challenging in the first place, as the complex valued $F_\perp$ in the single realizations shows very large differences after roughly 0.6s. However, a Larmor phase vortex is definitely observed in some single realizations. Probably the dynamics is very susceptible to the exact interplay of Larmor and spinor phase, and the creation of the vortex might pose a fine-tuning problem of the imprint, q_{eff} and the B–field gradient. The role of the latter is not yet fully understood. An idea for future measurements could be to initialize the system with a combination of spin wave and spinor phase imprint.

To build on the results of Section 5, investigating the effect of a spin wave in the initial condition without local imprint could help understanding the transition from the local density approximation to more complex dynamical behavior, and might also shed light on the role of the Larmor phase gradient on the creation of the vortex.

The connection to the instantons observed in [13] remains an open question. In the post–quench dynamics observed in that study, the vortices are preceded by rogue wave like events in the individual phase velocities. Realizing an analog initial condition in the experiment could also be a future project.

References

[1] J. Eisert, M. Friesdorf, and C. Gogolin. "Quantum many-body systems out of equilibrium". en. In: *Nature Physics* 11.2 (Feb. 2015). Publisher: Nature Publishing Group, pp. 124–130. ISSN: 1745-2481. DOI: 10.1038/nphys3215. URL: https://www.nature.com/articles/nphys3215 (visited on 06/20/2024).

[2] M. Gring et al. "Relaxation and Prethermalization in an Isolated Quantum System". In: *Science* 337.6100 (Sept. 2012). Publisher: American Association for the Advancement of Science, pp. 1318–1322. DOI: 10.1126/science.1224953. URL: https://www.science.org/doi/10.1126/science.1224953 (visited on 06/20/2024).

[3] Anatoli Polkovnikov et al. "Colloquium: Nonequilibrium dynamics of closed interacting quantum systems". In: *Reviews of Modern Physics* 83.3 (2011), p. 863.

[4] J. Berges et al. "Turbulent thermalization process in heavy-ion collisions at ultrarelativistic energies". In: *Physical Review D* 89.7 (Apr. 2014). Publisher: American Physical Society, p. 074011. DOI: 10.1103/PhysRevD.89.074011. URL: https://link.aps.org/doi/10.1103/PhysRevD.89.074011 (visited on 06/20/2024).

[5] J. Berges. *Nonequilibrium Quantum Fields: From Cold Atoms to Cosmology.* arXiv:1503.02907 [cond-mat, physics:hep-ph]. Mar. 2015. DOI: 10.48550/arXiv.1503.02907. URL: http://arxiv.org/abs/1503.02907 (visited on 06/20/2024).

[6] Vladimir E Zakharov, Victor S L'vov, and Gregory Falkovich. *Kolmogorov spectra of turbulence I: Wave turbulence.* Springer Science & Business Media, 2012.

[7] Christian Scheppach, Jürgen Berges, and Thomas Gasenzer. "Matter-wave turbulence: Beyond kinetic scaling". In: *Physical Review A* 81.3 (Mar. 2010). Publisher: American Physical Society, p. 033611. DOI: 10.1103/PhysRevA.81.033611. URL: https://link.aps.org/doi/10.1103/PhysRevA.81.033611 (visited on 06/14/2024).

[8] L. E. Sadler et al. "Spontaneous symmetry breaking in a quenched ferromagnetic spinor Bose–Einstein condensate". en. In: *Nature* 443.7109 (Sept. 2006). Publisher: Nature Publishing Group, pp. 312–315. ISSN: 1476-4687. DOI: 10.1038/nature05094. URL: https://www.nature.com/articles/nature05094 (visited on 06/20/2024).

[9] C. D. Hamley et al. "Spin-nematic squeezed vacuum in a quantum gas". en. In: *Nature Physics* 8.4 (Apr. 2012). Publisher: Nature Publishing Group, pp. 305–308. ISSN: 1745-2481. DOI: 10.1038/nphys2245. URL: https://www.nature.com/articles/nphys2245 (visited on 06/20/2024).

[10] J. Stenger et al. "Spin domains in ground-state Bose–Einstein condensates". en. In: *Nature* 396.6709 (Nov. 1998). Publisher: Nature Publishing Group, pp. 345–348. ISSN: 1476-4687. DOI: 10.1038/24567. URL: https://www.nature.com/articles/24567 (visited on 06/20/2024).

[11] Christian-Marcel Schmied et al. "Bidirectional universal dynamics in a spinor Bose gas close to a nonthermal fixed point". In: *Physical Review A* 99.3 (Mar. 2019). Publisher: American Physical Society, p. 033611. DOI: 10.1103/PhysRevA.99.033611. URL: https://link.aps.org/doi/10.1103/PhysRevA.99.033611 (visited on 06/14/2024).

[12] Maximilian Prüfer et al. "Observation of universal dynamics in a spinor Bose gas far from equilibrium". In: *Nature* 563.7730 (Nov. 2018). Publisher: Nature Publishing Group, pp. 217–220. ISSN: 1476-4687. DOI: 10.1038/s41586-018-0659-0. URL: https://www.nature.com/articles/s41586-018-0659-0 (visited on 05/27/2024).

[13] Ido Siovitz et al. "Universal Dynamics of Rogue Waves in a Quenched Spinor Bose Condensate". In: *Physical Review Letters* 131.18 (Nov. 2023). Publisher: American Physical Society, p. 183402. DOI: 10.1103/PhysRevLett.131.183402. URL: https://link.aps.org/doi/10.1103/PhysRevLett.131.183402 (visited on 06/14/2024).

[14] Yuki Kawaguchi and Masahito Ueda. "Spinor bose–einstein condensates". In: *Physics Reports* 520.5 (2012), pp. 253–381.

[15] Dan M Stamper-Kurn and Masahito Ueda. "Spinor Bose gases: Symmetries, magnetism, and quantum dynamics". In: *Reviews of Modern Physics* 85.3 (2013), p. 1191.

[16] Philipp Kunkel. "Splitting a Bose Einstein condensate enables EPR steering and simultaneous readout of noncommuting observables". PhD thesis. Universität Heidelberg, 2019.

[17] Stefan Lannig. "Vector Solitons and Different Scenarios of Universal Dynamics in a Spin-1 Bose-Einstein Condensate". PhD thesis. Universität Heidelberg, 2022.

[18] Lev P. Pitaevskii et al. *Bose-Einstein Condensation*. International Series of Monographs on Physics. Oxford, New York: Oxford University Press, Apr. 2003. ISBN: 978-0-19-850719-2.

[19] Shun Uchino. "Spinor Bose gas in an elongated trap". en. In: *Physical Review A* 91.3 (Mar. 2015), p. 033605. ISSN: 1050-2947, 1094-1622. DOI: 10.1103/PhysRevA.91.033605. URL: https://link.aps.org/doi/10.1103/PhysRevA.91.033605 (visited on 06/05/2024).

[20] Jochen Kronjäger. "Coherent dynamics of spinor Bose-Einstein condensates". PhD thesis. Staats-und Universitätsbibliothek Hamburg Carl von Ossietzky, 2007.

[21] Tim Langen, Thomas Gasenzer, and Jörg Schmiedmayer. "Prethermalization and universal dynamics in near-integrable quantum systems". en. In: *Journal of Statistical Mechanics: Theory and Experiment* 2016.6 (June 2016). Publisher: IOP Publishing and SISSA, p. 064009. ISSN: 1742-5468. DOI: 10.1088/1742-5468/2016/06/064009. URL: https://dx.doi.org/10.1088/1742-5468/2016/06/064009 (visited on 06/14/2024).

[22] Philipp Kunkel et al. "Simultaneous Readout of Noncommuting Collective Spin Observables beyond the Standard Quantum Limit". In: *Physical Review Letters* 123.6 (Aug. 7, 2019). Publisher: American Physical Society, p. 063603. DOI: 10.1103/PhysRevLett.123.063603. URL: https://link.aps.org/doi/10.1103/PhysRevLett.123.063603 (visited on 05/27/2024).

[23] Fam Le Kien, Philipp Schneeweiss, and Arno Rauschenbeutel. "Dynamical polarizability of atoms in arbitrary light fields: general theory and application to cesium". In: *The European Physical Journal D* 67 (2013), pp. 1–16.

[24] R. H. Leonard et al. "High-precision measurements of the Rb 87 D -line tune-out wavelength". In: *Physical Review A* 92.5 (Nov. 2, 2015), p. 052501. ISSN: 1050-2947, 1094-1622. DOI: 10.1103/PhysRevA.92.052501. URL: https://link.aps.org/doi/10.1103/PhysRevA.92.052501 (visited on 05/27/2024).

[25] R. H. Leonard et al. "Erratum: High-precision measurements of the Rb 87 D -line tune-out wavelength [Phys. Rev. A **92** , 052501 (2015)]". In: *Physical Review A* 95.5 (May 4, 2017), p. 059901. ISSN: 2469-9926, 2469-9934. DOI: 10.1103/PhysRevA.95.059901. URL: http://link.aps.org/doi/10.1103/PhysRevA.95.059901 (visited on 05/27/2024).

[26] Felix Schmidt et al. "Precision measurement of the Rb 87 tune-out wavelength in the hyperfine ground state F = 1 at 790 nm". In: *Physical Review A* 93.2 (Feb. 16, 2016), p. 022507. ISSN: 2469-9926, 2469-9934. DOI: 10.1103/PhysRevA.93.022507. URL: https://link.aps.org/doi/10.1103/PhysRevA.93.022507 (visited on 05/27/2024).

[27] David Feiz Bakhsh Bazargani. "Noise reduction of local spin rotations and analysis of the three-component vector soliton formation". Masterarbeit. Universität Heidelberg, 2023.

[28] Maximilian Prüfer. *Experimentally testing quantum field theory concepts with spinor Bose gases far from equilibrium*. eng. Dissertation. Place: Heidelberg. 2020. DOI: 10.11588/heidok.00027925. URL: https://archiv.ub.uni-heidelberg.de/volltextserver/27925/ (visited on 06/06/2024).

[29] François Riggio et al. "Gradient corrections to the local-density approximation in the one-dimensional Bose gas". In: *Physical Review A* 106.5 (Nov. 2022). ISSN: 2469-9934. DOI: 10.1103/physreva.106.053309. URL: http://dx.doi.org/10.1103/PhysRevA.106.053309.

[30] Maximilian Prüfer et al. "Condensation and thermalization of an easy-plane ferromagnet in a spinor Bose gas". en. In: *Nature Physics* 18.12 (Dec. 2022). Publisher: Nature Publishing Group, pp. 1459–1463. ISSN: 1745-2481. DOI: 10.1038/s41567-022-01779-6. URL: https://www.nature.com/articles/s41567-022-01779-6 (visited on 06/06/2024).

[31] Lawrence F Shampine and Mark W Reichelt. "The matlab ode suite". In: *SIAM journal on scientific computing* 18.1 (1997), pp. 1–22.

A Simulation SMA

To gain a better insight into the spin dynamics on the spin–nematic sphere, some simulated trajectories are presented here, together with the time resolved Q_0–oscillation and the sinusoidal fit (see Fig. 23). Shown are three trajectories starting at an elongated spin ($S_x = 1$) corresponding to $\phi_s^{IC} = 0$, for different values of q/nc_1. The EOM 18 and 19 are solved with an ODE solver [31].

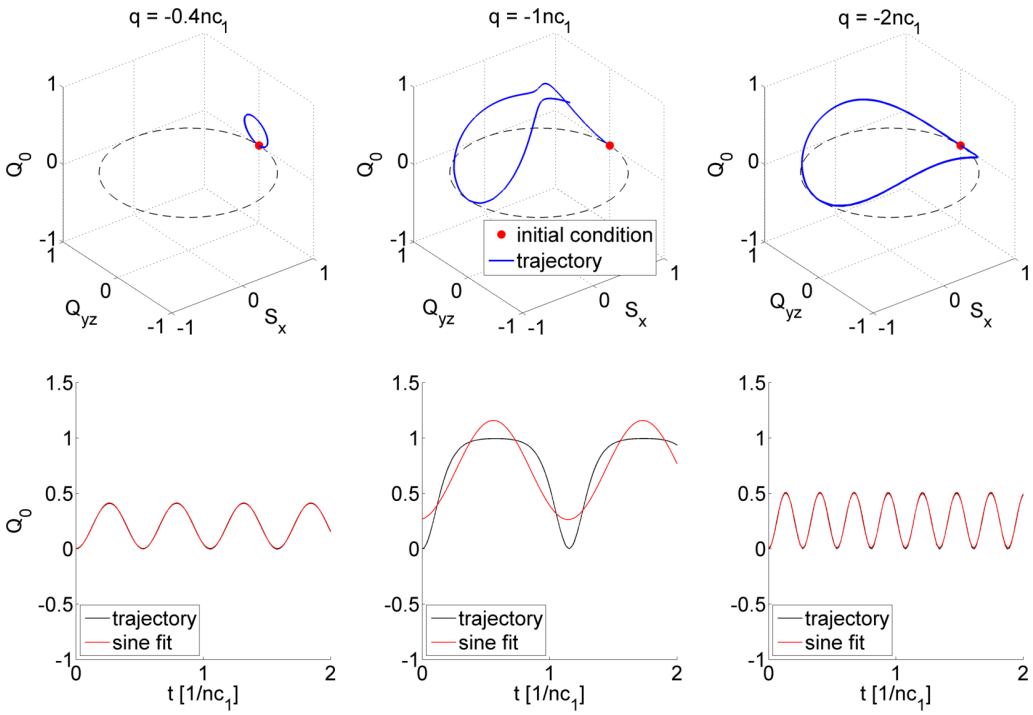

Figure 23: Upper panel: trajectories on the spin–nematic sphere for different q. The IC is always chosen to be $\phi_s^{IC} = 0$ (indicated by the red dot) and $nc_1 = -1$. Lower panel: $Q_0(t)$ (black) for the three trajectories above. In red, the sinusoidal fit function $Q_0^{\text{fit, sim}}(t) = A \cdot \sin(2\pi(ft + c)) + d$ is shown. One can see, that trajectories close to the seraratrix deviate from the sinusoidal shape. The frequency is obtained from the sine fit using a very narrow window for f, determined by the temporal spacing of the minima and maxima in $Q_0(t)$. The offset is the maximal value minus the minimal value of the simulated trajectory, and the amplitude is the maximal value minus the offset. This method allows to circumvent the systematic errors in the fit close to the separatrix, especially for the offset. The numbers for q are rounded to the first decimal. A state starting at exactly $\phi_s^{IC} = 0$ lies exactly on the separatrix for $q = -1nc_1$, so that it would never reach the north pole of the spin–nematic sphere.

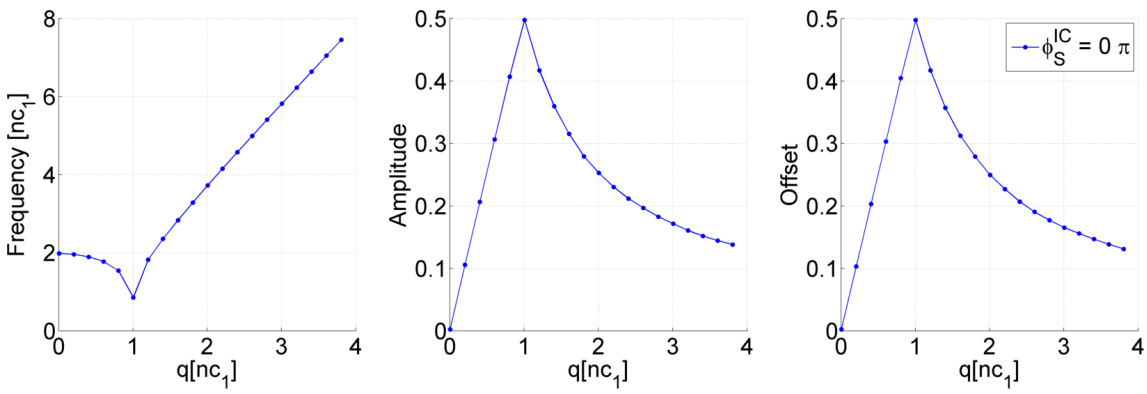

Figure 24: Frequency, amplitude and offset (left to right) for the same IC ($\phi_s^{IC} = 0$), and different q/nc_1. The frequency goes down as the state changes from trapped (low q) to free–running (large q). For large q, the frequency is approximately given as $f = 2q$. The offset shows the linear behavior derived in equation 24 for the stable point in Q_0. This linear behaviour is given for all trapped oscillations independent of q/nc_1 and ϕ_s^{IC}.

B Additional plots to Section 5

Fig. 25 shows additional plots capturing the evolution of different spatially flat spin profiles under different values for the second–order Zeeman shift q_{exp}. In Section 5, three trapped trajectories are analyzed. In addition to these, a trajectory very close to the stable point is seen (upper panel), and different free–running trajectories (lower three panels). None of the measurements shows an excitation of spatial modes.

Fig. 26 shows cuts through the oscillations and depicts the trajectory on the $F_\perp$–q_0–plane. Note that free–running trajectories cannot be identified by negative $F_\perp$ in the experiment, as it is per definition positive. An indication for a free–running trajectory is that $F_\perp(t)$ goes (almost) to zero. The quickest way to identify a free–running trajectory is to look at the spatial dependence of the oscillation frequency. As the density is higher in the center (and therefore nc_1), free–running trajectories feature a slower oscillation in the center than towards the edge. Trapped oscillations show the opposite behavior. If a state locally changes from trapped to free–running, the larmor phase helps to identify different spin orientations. Note that for states featuring a larmor phase gradient, the sign of this gradient does not change for free running trajectories, as one could naively expect.

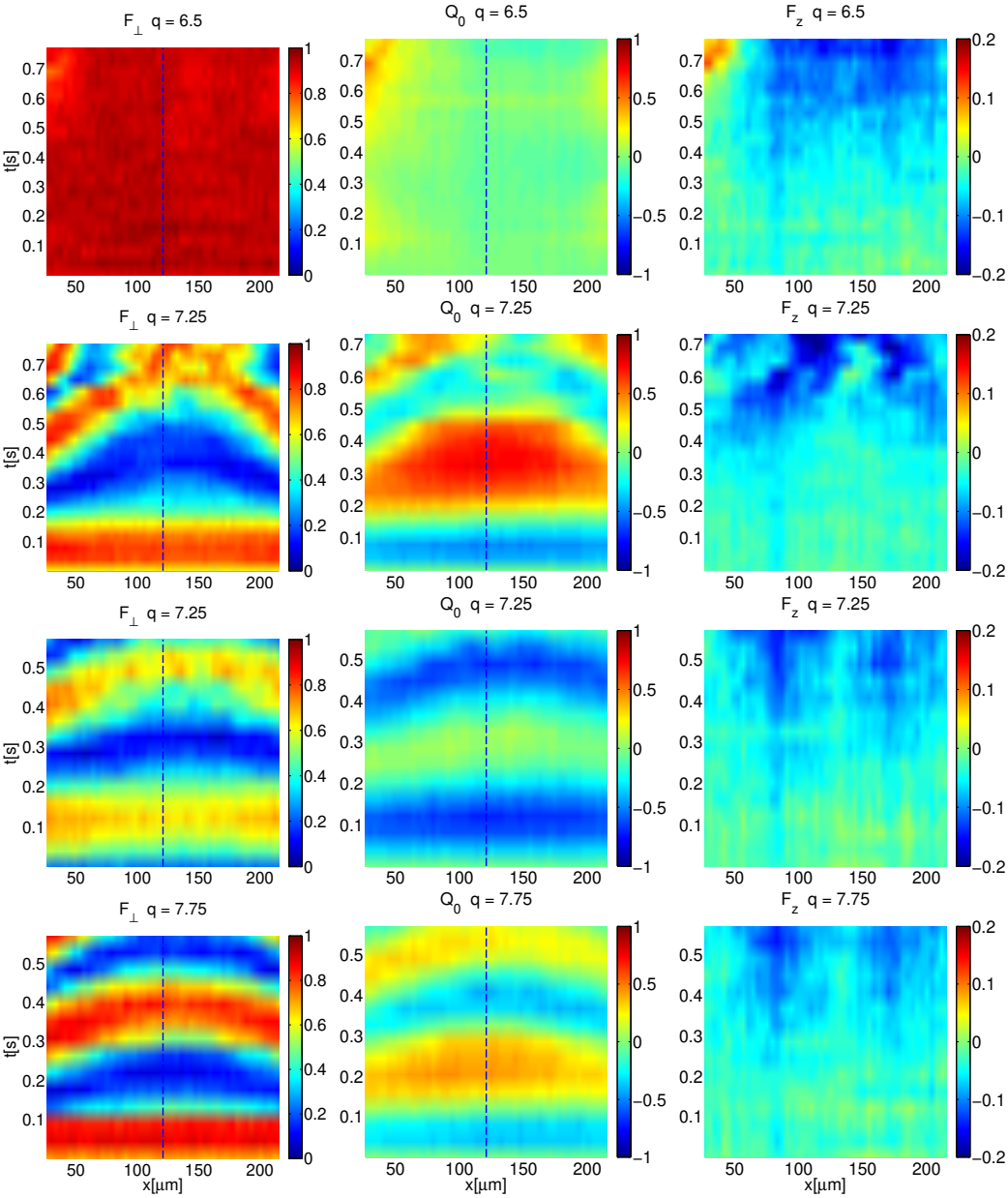

Figure 25: Each plot shows the time evolution of measured spin observables, with space on the x–axis and evolution time on the y–axis, averaged over ∼12 realizations. The three columns show $F_\perp$, Q_0 and F_z (left to right). Each row shows the time evolution of one specific initial condition, for one specific q_{exp}, respectively (denoted by q in the captions).

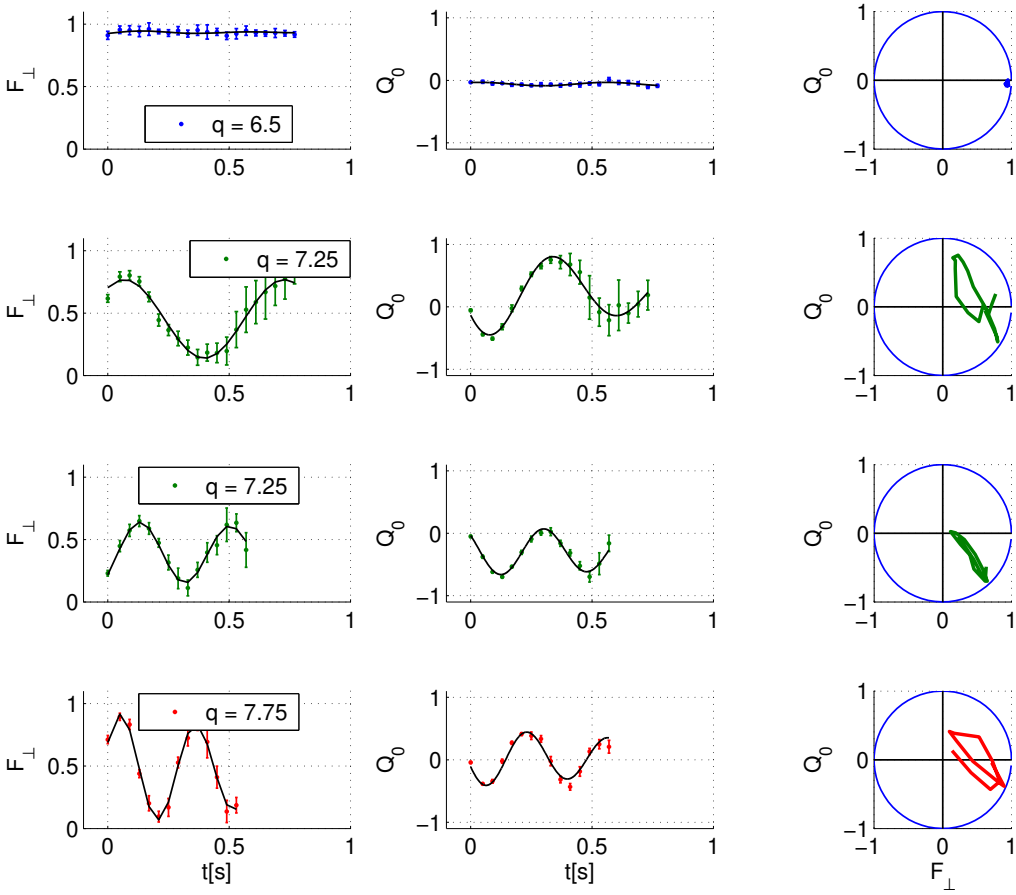

Figure 26: Left and middle: Cuts through the time evolution of the measured $F_\perp$ and Q_0 profiles at a single spatial position $x_{\text{cut}} \pm \Delta x$ with ($\Delta x \approx 4\mu\text{m}$ given by the bin size). The black line in each plot represents a fit function. The functional shape of the fit function for $Q_0(t)$ is given by 36. The fit to $F_\perp$ is not used. Each row presents one setting for q_{exp} (denoted by q in the labels). The right panel shows the trajectory on a projection of the spin–nematic sphere on the $F_\perp$–Q_0–plane. Error bars indicate the standard deviation of the single realizations. Upper most panel shows the trajectory of a state of the stable point. All other panels show free–running oscillations. Experimental measurement data are always in the right quadrants of the $F_\perp$–Q_0–plane, as $F_\perp$ is always positive. That makes it harder to identify free–running trajectories.

C Additional plots to Section 6.3

As mentioned in section 6.3, the single realizations in this measurement differ increasingly, especially after roughly 0.6s, where the sharp dip in $|F_\perp|$ occurs. $\langle |F_\perp| \rangle$ (left) and $|\langle F_\perp \rangle|$ (center) are shown in Fig. 27. The right panel shows the square root of the variance of the single realizations in the complex $F_\perp$.

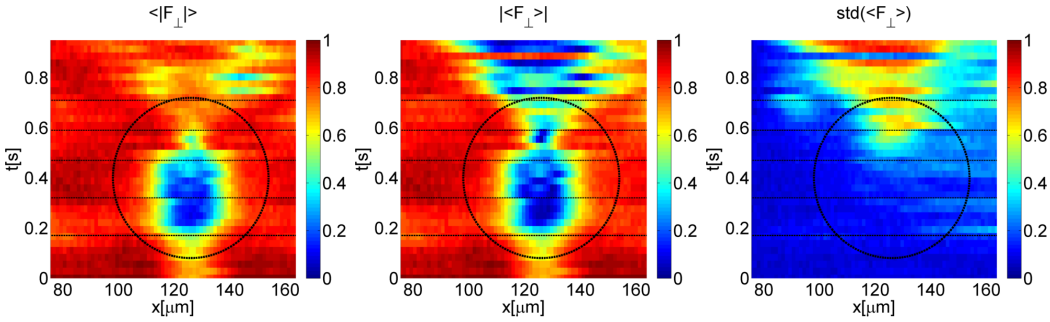

Figure 27: Left: First taking the absolute value $|F_\perp|$ and then averaging allows to see how elongated the spin is in average. Center: First averaging the complex valued $F_\perp$ and then taking the absolute value causes the the single realizations to average to very low values after ~ 0.59s. This region gets increasingly larger. Right: The standard deviation of the complex single realizations clearly shows the diverging behavior of the single realizations.

Acknowledgements

At this point I would like to express my gratitude to everyone who supported and accompanied me during the last year.
First and foremost, I want to thank Markus for giving me the opportunity to work on this exciting project in his group. His enthusiasm and curiosity really inspired and motivated me.
I also want to express my gratitude to Yannick, who introduced me to the experiment and answered countless questions, and Alex, who was always very interested in what I did and helped me with good ideas wherever he could. Thanks also to Helmut who never hesitated to take some time to answer my questions or help out in the lab. You were a great team to work with. It was not only good work, but also really fun! This goes to the whole matterwavers group - I really enjoyed the time with all of you.
I also want to thank Thomas for taking the role as the second supervisor of this thesis. Thanks also to Ido, who supported us from the theory side with a lot of effort.
Finally I want to thank my friends and family. Your support, patience and love helped me in everything I did.

Erklärung:

Ich versichere, dass ich diese Arbeit selbstständig verfasst habe und keine anderen als die angegebenen Quellen und Hilfsmittel benutzt habe.

Heidelberg, den (Unterschrift)

.....